https://doi.org/10.5194/egusphere-2026-7079
Preprint. Discussion started: 24 November 2026
© Author(s) 2026. CC BY 4.0 License.

Sea Ice Thickness Below Melt Ponds

Maximilian Harald Ringel[1], Janna Elisabeth Rückert[1], David Clemens-Sewall[2], Dmitry Divine[3], Marcel Nicolaus[4], Melinda Webster[5], and Gunnar Spreen[1]

[1]University of Bremen, Institute of Environmental Physics, Bremen, Germany
[2]University of Colorado Boulder, Institute for Arctic and Alpine Research, Boulder, CO, USA
[3]Norwegian Polar Institute, Fram Centre, Tromsø, Norway
[4]Alfred-Wegener-Institut, Helmholtz-Zentrum für Polar- und Meeresforschung, Bremerhaven, Germany
[5]University of Washington, Applied Physics Laboratory, Polar Science Center, Seattle, WA, USA

Correspondence: Maximilian Harald Ringel (mringel@uni-bremen.de)

Abstract. Arctic summer sea ice thickness (SIT) remains difficult to observe because surface melt complicates satellite retrievals. Ice beneath melt ponds is particularly relevant: ponds cover substantial fractions of summer sea ice, influence ocean light transmission, and are excluded from emerging summer altimetry retrievals. Optical estimates of under-pond SIT can complement these products.

We analyze 67 hyperspectral melt pond images (400–900 nm) with co-located under-pond SIT measurements (0.17–2.83 m), collected during the *CONTRASTS* expedition (*PS149*) aboard research vessel *Polarstern* in the central Arctic Ocean in July–August 2025. This is the largest such observational dataset to date. Melt pond reflectance and color strongly relate to under-pond SIT, with relationships depending on pond-bottom structure. Bottoms containing air bubbles show a logarithmic reflectance increase below 1 m ice thickness and saturation above, whereas homogeneous (bubble-free) bottoms exhibit a near-linear increase across the observed thickness range. A spectral slope criterion at 690–730 nm distinguishes these bottom types, enabling more accurate pond bottom-specific retrieval models. Radiative transfer simulations reproduce observations for mixed pond-bottom conditions but cannot reproduce the linear relationship for homogeneous bottoms.

Bivariate regressions using YIQ (Y: Luma, I: In-Phase, Q: Quadrature) color components derived from RGB images to retrieve under-pond SIT yield R^2 values of 0.85 for homogeneous bottoms, 0.31 for bubbly bottoms, and 0.64 for both types combined, with RMSE values of 0.30–0.42 m. These results demonstrate the potential of optical observations to complement summer SIT measurements over ponded ice surfaces and support retrievals using RGB sensors on drones, aircraft, and satellites.

1 Introduction

Sea ice thickness (SIT) is one of the fundamental parameters characterizing the Arctic sea ice cover. As an essential climate variable SIT plays a critical role in climate dynamics as well as in the Arctic surface energy and mass balance (Landrum and Holland, 2022). It is further important for marine ecosystems (Akino et al., 2025), and human activities in polar regions. Over recent decades, Arctic SIT has decreased substantially alongside the well-documented decline in sea ice extent (Stroeve and Notz, 2018). While Notz and Stroeve (2016) showed an overall negative linear response of Arctic sea ice extent to global CO_2 forcing, sea ice thickness changes can exhibit abrupt non-linear regime shifts as observed in the Fram Strait by Kacimi and

https://doi.org/10.5194/egusphere-2026-7079
Preprint. Discussion started: 24 November 2026
© Author(s) 2026. CC BY 4.0 License.

Kwok (2024). Continuous year-round observations of SIT are therefore essential to monitor these ongoing changes, to validate climate models, and to improve projections of future Arctic conditions (Sumata et al., 2023).

During winter, pan-Arctic SIT observations are primarily derived from satellite radar (e.g., *CryoSat*) and laser altimeters (e.g., *ICESat-2*), which infer SIT from freeboard estimates (Laxon et al., 2013; Petty et al., 2020) and perform best for ice thicker than 1 m. For thinner ice (<0.5 m), L-band passive microwave radiometry is usually preferred (Tian-Kunze et al., 2014; Huntemann et al., 2014; Paţilea et al., 2019). Thermal infrared and synthetic aperture radar approaches are limited to thin ice or rely on assumptions about the relationship between backscatter and sea ice thickness (Yu and Rothrock, 1996; Karvonen et al., 2012). During summer, meltwater and wet snow invalidate key retrieval assumptions, making most standard methods unreliable. Consequently, there is a consistent gap across most pan-Arctic SIT observations for the four melting season months of June to September.

Recent altimetry advances have begun to bridge this gap. Dawson et al. (2022) used a neural network to distinguish melt ponds from open-water leads in *CryoSat-2* observations. This enables year-round SIT estimates when combined with an all-season snow-load model (Landy et al., 2022). Petty et al. (2026) extended this framework to *ICESat-2*, reporting summer root mean square errors (RMSE) of about 0.38 m against sonar draft and buoy estimates. To date, the methods of Landy et al. (2022) and Petty et al. (2026) remain the only two satellite-derived pan-Arctic summer SIT estimates.

Local and regional summer observations include airborne electromagnetic surveys using the EM-Bird, with an accuracy of about ±0.1 m over flat ice but underestimation over ridges and keels (Haas and Jochmann, 2003; Haas et al., 2009; Pfaffling et al., 2007), and airborne laser altimetry measuring snow plus ice freeboard, with accuracies of ±0.22–0.7 m after conversion to ice thickness (Kurtz et al., 2013). Upward-looking sonars measure ice draft with uncertainties of ±0.1–0.25 m (Melling and Riedel, 1995; Rothrock and Wensnahan, 2007), with moorings providing long time series at fixed locations (Sumata et al., 2023; Spreen et al., 2020). In situ drillings provide accurate reference measurements, while ground-based electromagnetic surveys extend spatial coverage along transects. Latter ones yield SIT estimates within 5–10% uncertainty compared to drill hole SIT measurements (Haas et al., 1997). Overall, the absolute accuracy, uncertainty, and RMSE values reported above span approximately 0.1–0.7 m, although they describe different error metrics. Despite their accuracy, these observations have insufficient spatial coverage to characterize Arctic-wide summer SIT variability and evolution, motivating additional retrieval concepts.

One such concept is the topic of this manuscript: optical remote sensing of sea ice beneath melt ponds, hereafter referred to as under-pond SIT. Melt ponds can cover up to 30–40% of the Arctic sea ice area toward the end of the melt season (Lee et al., 2024; Niehaus et al., 2024; Istomina et al., 2025) and provide a potential window into the underlying ice because they are optically coupled to it (Grenfell and Perovich, 1984; Perovich et al., 1998). Their reflectance spectra exhibit high reflectance at short visible wavelengths, a transitional decrease, and low reflectance in the near-infrared. Between 400 and 600 nm, water

https://doi.org/10.5194/egusphere-2026-7079
Preprint. Discussion started: 24 November 2026
© Author(s) 2026. CC BY 4.0 License.

absorption is minimal and light is predominantly scattered by the pond bottom, allowing reflectance to reach values comparable to bare sea ice (Light et al., 2015; Malinka et al., 2018). Within this range, melt pond albedo and reflectance increase strongly with under-pond SIT (Istomina et al., 2016; Lu et al., 2016; Malinka et al., 2018; Xiong and Ren, 2023). Above approximately 750 nm, water absorption becomes dominant and largely obscures the pond bottom. Pond water depth generally plays a smaller role in melt pond reflectance and albedo than under-pond SIT (Perovich, 2003; Lu et al., 2016, 2018; Malinka et al., 2018; Zhang et al., 2022). Note that this study focuses on spectral melt pond reflectance, whereas other studies examine melt pond albedo. Although these quantities differ in their definitions, they are closely related, and we therefore occasionally use the terms interchangeably when comparing our findings with previous work.

Previous studies explored the sensitivity of melt pond reflectance and color to SIT (Istomina et al., 2016; Lu et al., 2018; Malinka et al., 2018; Zhang et al., 2021). Istomina et al. (2016) identified an empirical relationship between under-pond SIT and hue, saturation, and lightness extracted from 17 RGB (R: Red, G: Green, B: Blue) images. Using radiative transfer simulations, Lu et al. (2018) demonstrated positive correlations between under-pond SIT and RGB intensities, particularly in the green and blue channels. Zhang et al. (2022) evaluated three retrieval models against six observational datasets and found that the Malinka et al. (2018) model performed best, with R = 0.79 and a mean absolute error of 0.12 m. However, observational validation remains limited by the small number and restricted thickness range of available co-located optical and under-pond SIT measurements.

Besides thickness, the scattering properties of the pond bottom strongly influence melt pond reflectance. Bubble-rich (hereafter referred to as "bubbly") ice has long been described as “milky,” with higher visible reflectance than homogeneous ice (Grenfell and Perovich, 1984). During the SHEBA expedition 1997–1998 (Welch, 1998), “white ponds” were attributed to high bubble fractions in the underlying ice (Perovich et al., 1998; Perovich and Polashenski, 2012). Perovich et al. (2002) documented a pond with light and dark sections at identical water depths, attributing the higher albedo of the lighter section to greater air bubble abundance. Malinka et al. (2018) retrieved transport scattering coefficients more than five times higher for bubbly than homogeneous pond bottoms. Air bubbles scatter light more efficiently than brine inclusions because the refractive index contrast is much larger at the air–ice interface than at the brine–ice interface (Thomas, 2025). This difference in scattering efficiency is consistent with the finding by Xiong and Ren (2023) that brine inclusions have a weaker influence on melt pond reflectance than air bubbles. Light et al. (2008) attributed bright, bubbly pond bottoms to former snow-covered ice surfaces retaining highly scattering microstructure. Darker, homogeneous bottoms originate from interior ice, which has a much lower scattering coefficient than the surface scattering layer (Light et al., 2008). These structural differences must therefore be considered when investigating the melt pond reflectance–SIT relationship.

An optical retrieval would provide thickness estimates only for the ponded fraction of the ice surface, complementing summer altimetry retrievals that exclude ponded surfaces (Landy et al., 2022; Petty et al., 2026). Under-pond SIT is also relevant to ecosystem studies because melt ponds increase the transmission of photosynthetically active radiation into the ocean (Nicolaus

https://doi.org/10.5194/egusphere-2026-7079
Preprint. Discussion started: 24 November 2026
© Author(s) 2026. CC BY 4.0 License.

et al., 2012; Katlein et al., 2014; Lu et al., 2016), supporting primary production beneath the ice (Arrigo et al., 2012; Oziel et al., 2019; Ardyna et al., 2020a, b).

Here, we analyze 67 hyperspectral images (400–900 nm) of melt ponds with co-located under-pond SIT and pond depth measurements collected during the *CONTRASTS* expedition on RV *Polarstern* (*PS149*, July–August 2025; Nicolaus (2026); Ringel et al. (2026)). This dataset is considerably larger than previous datasets (listed in Tab. 1), spans under-pond SIT of 0.2–2.8 m, and includes ponds on first-year, second-year, and multiyear ice. We introduce the dataset in more detail in Sect. 2 before using it to investigate the relationship between melt pond reflectance and under-pond SIT in Sect. 3. We compare the observed relationship with radiative transfer simulations (Sect. 3.1.1) and examine how pond-bottom structure affects it (Sect. 3.1.2). In Sect. 3.2 we then examine the relationship between melt pond color and under-pond SIT for the RGB (Sect. 3.2.1) and YIQ (Y: Luma, I: In-Phase, Q: Quadrature, Sect. 3.2.2) color spaces. Based on these analyses, we present an empirical SIT retrieval approach that can serve as a basis for under-pond SIT retrievals from airborne and spaceborne platforms in Sect. 4.

2 Data & methods

2.1 Field observations

2.1.1 The *CONTRASTS* expedition

The RV *Polarstern CONTRASTS* expedition (*PS149*) was a two-month ship-based expedition in the central Arctic Ocean, north of Svalbard and Greenland, with the German research vessel (RV) *Polarstern* from 2 July 2025 to 1 September 2025. The expedition focused on three distinct ice floes which represent the first-year ice (FYI), the second-year ice (SYI) and multiyear ice (MYI) regimes. These three regimes are intended to represent the future, present and past Arctic ice regime, respectively. The three ice floes were visited up to four times by going in consecutive rounds with RV *Polarstern*. The SYI- and MYI-floe were visited in all four rounds while the FYI-floe was only visited in the first two rounds before it broke apart due to melting. In the 3rd round a FYI-floe in the same ice regime with similar properties to the original FYI-floe was measured as a replacement. This replacement floe was not visited again in round four. Each floe visit consisted of at least two, normally three days of ice station measurements for which the ship was anchored to the floe. This means *CONTRASTS* offered the unique possibility of measuring a large variety of melt ponds across the three typical Arctic ice regimes over a two month period at the climax of the melt season processes. For more detailed information about the expedition see the cruise report of Nicolaus (2026).

2.1.2 Melt pond reflectance observations

During the *CONTRASTS* expedition two-dimensional hyperspectral imaging of selected melt ponds at all floe visits was carried out using the portable hyperspectral pushbroom camera *Specim IQ* from *Specim LTD* operated in a nadir-viewing tripod

https://doi.org/10.5194/egusphere-2026-7079
Preprint. Discussion started: 24 November 2026
© Author(s) 2026. CC BY 4.0 License.



Figure 1. The tripod configuration used for the measurements of dataset Ringel et al. (2026). The *Specim IQ* hyperspectral camera is mounted at a nadir-viewing angle toward the melt pond within the upper-left protective case. The right case is used as a counterweight. Using this tripod configuration, the camera is about 2.80 m above the melt pond bottom.

configuration (Fig. 1). This configuration consisted of the *Specim IQ* camera mounted on a tripod within a protective case, an outdoor tablet for remote camera operation, and a white reference plate. The camera was mounted in a nadir-looking position using a smaller lateral tripod arm on top of the bigger tripod. A counter weight on the other side of the lateral tripod arm balanced the camera. This tripod configuration provided a camera height of around 2.80 m in its full extension and about 0.5 m lateral displacement from the tripod head. The camera incidence and roll angle were manually aligned to about 90° and 0°, respectively. For more technical details about the used configuration see Nicolaus (2026), Chapter 2.5.

The *Specim IQ* camera records 204 spectral bands over the visible (VIS) to near-infrared (NIR) wavelength range from 400 nm to 1000 nm with a spectral resolution of about 7 nm. Each hyperspectral image has a resolution of 512×512 pixels, resulting in a data cube comprising 204×512×512 data points. The camera was operated in the so-called *simultaneous white-reference* mode. In this mode, each measurement consists of three co-registered acquisitions at identical exposure settings: the scene

https://doi.org/10.5194/egusphere-2026-7079
Preprint. Discussion started: 24 November 2026
© Author(s) 2026. CC BY 4.0 License.

radiance, the radiance of the white-reference panel placed within the field of view, and a dark reference recorded with the lens shutter closed to characterize the sensor's thermal and electronic background signal. Relative spectral reflectance is derived by (a) subtracting the dark reference from both the scene and white reference signals, and thereafter (b) computing their ratio. This yields a dimensionless quantity, reflectance, that ideally is independent of illumination intensity and sensor exposure time, and thus directly comparable across all acquisitions in the dataset. Exposure times were mostly set to approximately 2 ms. At this short exposure time the spectral measurements from wavelengths greater than 900 nm have proven to be noisy. Accordingly, all measurements above 900 nm are excluded from further analysis. The opening angle of the camera, and thus its field of view, is about 31 degrees. At a tripod height of about 2.80 m this results in an image size of about 1.5 m by 1.5 m at the melt pond bottom.

The white reference is a ceramic plate which was mounted horizontally level on a small tripod and positioned in the lower right corner of each hyperspectral image (Fig. 2). As the reference for reflectance it is assumed to reflect all incident diffuse sunlight. Therefore, all measured spectral reflectance values presented and discussed here are given relative to the spectral reflectance measured at the white reference. To reduce the influence of noise on each reference spectrum, a mean spectrum averaged over a 20 x 20 pixel area is used as the reference spectrum. In the following, we refer to the described hyperspectral images as measurements or observations.

In total, 146 hyperspectral images were collected during *CONTRASTS* using the described tripod configuration (Ringel et al., 2026). Of these 146 images, 67 are co-located with under-pond SIT and melt pond depth measurements. Accordingly, this study is based on these 67 melt pond images. The 67 measurements were taken at 12 distinct melt ponds with repeat measurements of the same melt ponds during the consecutive floe visits. The observed melt ponds were chosen by their apparent color and melt pond bottom structure to ensure a variety of melt pond properties and under-pond SIT values. Consequently, the observed distributions of under-pond SIT, melt pond depth as well as the pond bottom structures are not necessarily statistically representative of the mean melt pond conditions of the visited floes.

From each of the 67 hyperspectral images a reflectance spectrum along with its standard deviation is derived by averaging over a manually specified sub-area of the total image as area 1 in Fig. 2 (black rectangle). For nearly all images the same area is selected (x-pixel range: 50–450, y-pixel range: 50–250) to ensure a comparable amount of pixel values for each reflectance spectrum. For some images the area had to be adjusted to ensure that features such as sea ice surfaces or the tripod legs are included. As mentioned in Sect. 1 melt pond bottoms often include air bubbles enclosed within the ice. These bubbly areas can spread over large surface fractions of the melt pond bottom. Figure 2 demonstrates that the reflectance of the bubbly pond bottom area (area 3, orange) is up to three times higher than the reflectance of the homogeneous pond bottom area (area 2, blue). Figure 3 demonstrates that such bright bottom areas do indeed contain air bubbles by showing two ice cores of the same heterogeneous melt pond bottom. While the ice core taken at the bright bottom area (Fig. 3a) contains many millimeter-sized round-shaped air inclusions (Fig. 3b & c) the ice core taken at the homogeneous bottom area (Fig. 3d) does not contain these small air inclusions (Fig. 3e & f). The larger centimeter-scaled air inclusions are brine inclusions.

https://doi.org/10.5194/egusphere-2026-7079
Preprint. Discussion started: 24 November 2026
© Author(s) 2026. CC BY 4.0 License.

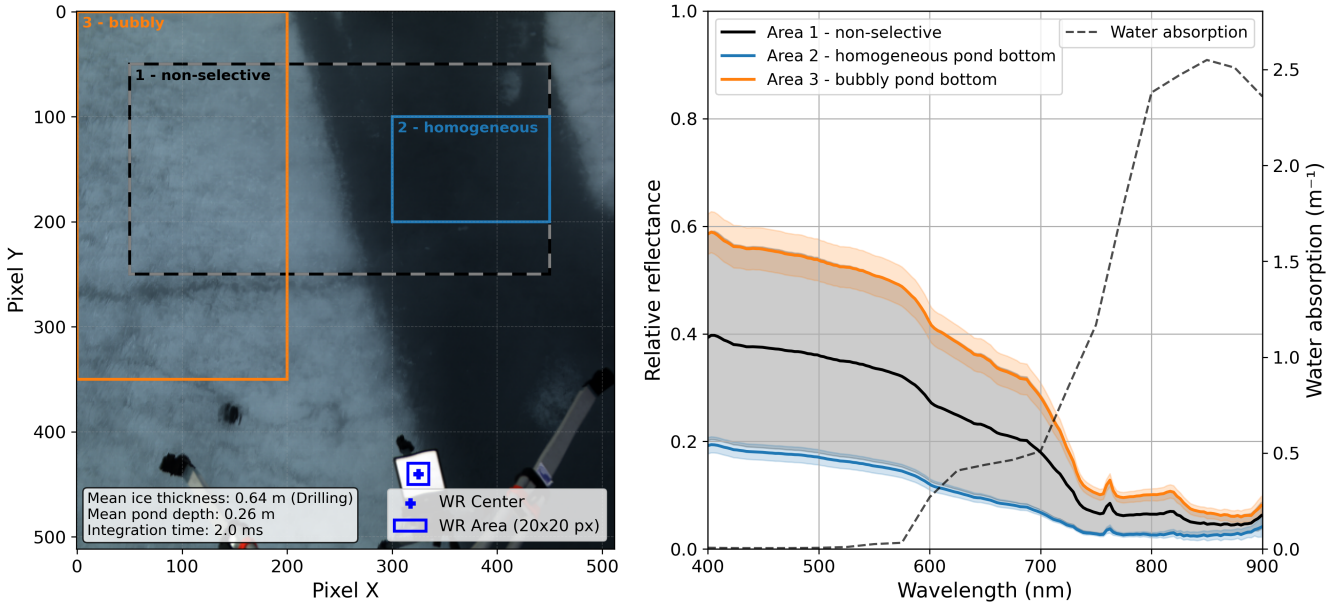

Figure 2. Left: RGB composite from a hyperspectral image (*PS149_2025-07-31_009*) taken by the *Specim IQ* camera during the CONTRASTS expedition on the SYI-floe (2nd visit). The colored and numbered rectangles visualize the default area in dashed black-gray (for better visibility) used for the non-selective measurements while the orange and blue areas denote the selection for bubbly and homogeneous pond bottom pixels, respectively. The "WR area" indicates the 20 x 20 pixel area over which the white reference spectrum was averaged and "WR center" the center pixel of this area. Right: The averaged reflectance spectra along with their color-shaded standard deviations for the corresponding areas shown in the left RGB image. The dashed line displays the absorption coefficient of clear seawater (Smith and Baker, 1981).

It is crucial to entangle these different reflectance behaviors of bubble-free (homogeneous) and bubbly pond bottoms in our following analyses. We define up to two additional areas in each image which contain only homogeneous pond bottom or only bubbly pond bottom, depending on the presence and surface area fraction of bubbly pond bottom within the individual image. Area 1 is considered to be the default area and, therefore, includes a random mix of pond bottoms. Consequently, in some cases area 1 also contains only homogeneous or only bubbly pond bottom. The reflectance spectra derived from area 1 are categorized as "non-selective" from here on. This naming emphasizes that area 1 is our fixed standard sampling area, not manually selected for specific bottom structure — in contrast to areas 2 and 3, which are specifically chosen to contain only homogeneous or only bubbly pond bottom (see Figure 2). Accordingly, this method creates three datasets of melt pond reflectance spectra, defined by their pond bottom structures: Non-selective pond bottom (67 measurements), homogeneous pond bottom (38 measurements) and bubbly pond bottom (29 measurements). Each reflectance spectrum is divided by the cosine of the sun elevation angle to make the measurements at different sun elevations more comparable. During the CONTRASTS expedition sun elevation angles were close to 30° start of July decreasing to about 10-15° end of August. The *CSV* table in the Appendix (Sec. 5) list

https://doi.org/10.5194/egusphere-2026-7079
Preprint. Discussion started: 24 November 2026
© Author(s) 2026. CC BY 4.0 License.

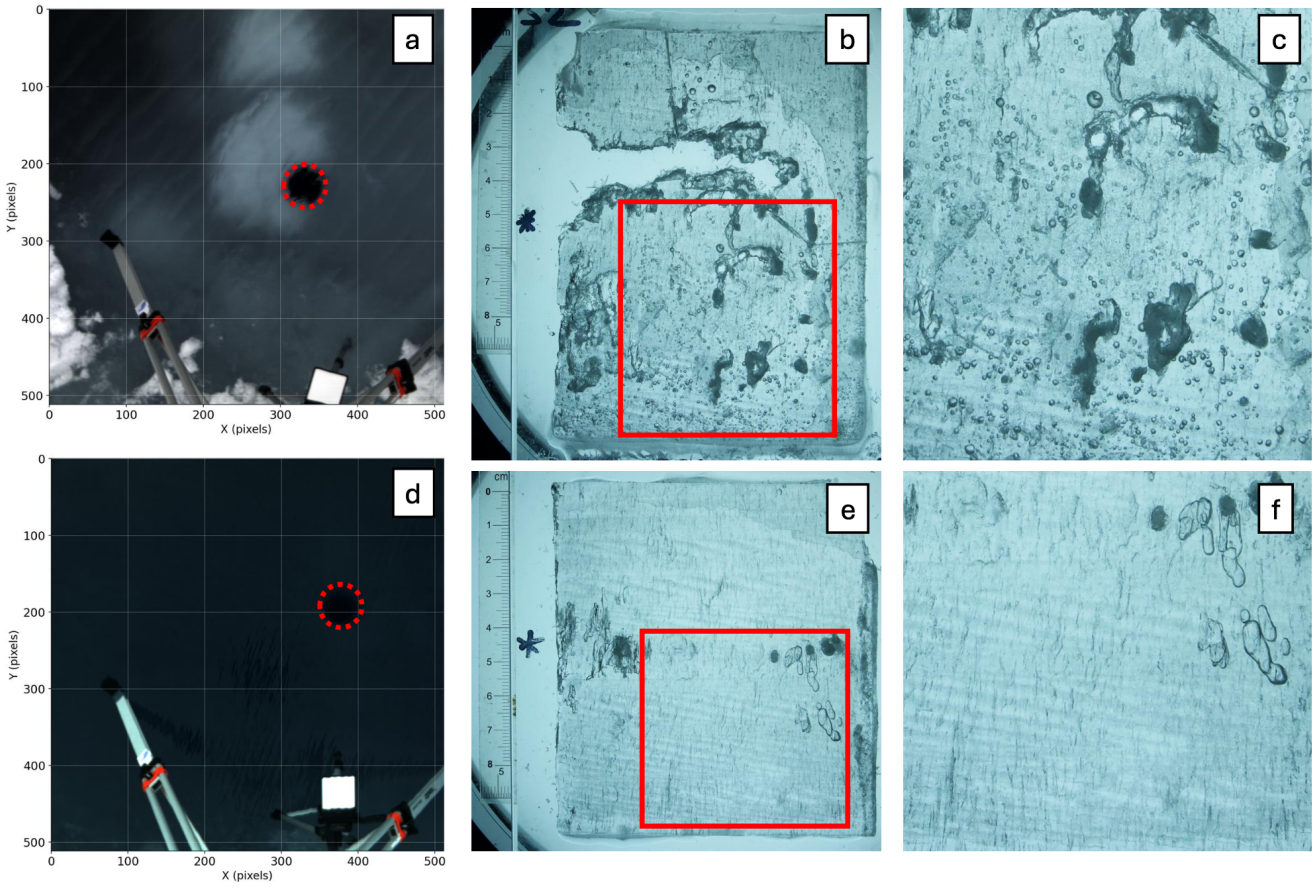

Figure 3. Sub-figures a and d show RGB composites of hyperspectral images each with a co-located coring site (indicated by the red dashed circle) within the image frame. Sub-figures b and e show thick sections of the corresponding ice cores. The red rectangles show the area of the zoomed-in images shown in sub-figures c and f. The image IDs of a and c are *PS149_2025-07-30_021* and *PS149_2025-07-30_023*, respectively. The site IDs of the images and corings are *neTransmittancePond* and *sTransmittancePond*, respectively.

all image IDs for the three datasets, along with the local floe coordinates of each measurement and the pixel coordinate ranges of the selected areas.

2.1.3 Melt pond depth and ice thickness observations

Co-located with each measured reflectance spectrum (Sect. 2.1.2) the corresponding melt pond depth and under-pond SIT was measured. The melt pond depth was measured by a meter stick at least three times within the image area. For the analysis here we use the averaged melt pond depth values.

The under-pond SIT was measured by two different methods. The first method was melt pond bottom drillings, which were usually conducted only once close to or within the image area.

https://doi.org/10.5194/egusphere-2026-7079
Preprint. Discussion started: 24 November 2026
© Author(s) 2026. CC BY 4.0 License.

In melt ponds which could not be drilled (to keep them intact for the following visits), the second method, a *Geophex GEM-2-730* instrument (in the following referred to as *GEM*) was used to measure the under-pond SIT via apparent electrical conductivity and magnetic susceptibility of the seawater. The instrument comprises a transmitter and receiver coil, separated by a constant spatial offset, and is operated at a fixed set of frequencies. We used the frequency set which was also used during the *MOSAiC* expedition (Itkin et al., 2023; Hendricks et al., 2022): 1525 Hz, 5325 Hz, 18325 Hz, 63025 Hz, and 93075 Hz. The transmitter generates a time-harmonic electromagnetic field with a frequency of 5 Hz that penetrates non-saline sea ice and induces eddy currents in the electrically conductive seawater beneath. These currents produce a secondary electromagnetic field, which is detected by the receiver and analyzed in terms of its in-phase and quadrature components. Because the conductivity of seawater is orders of magnitude higher than that of sea ice and snow, the measured electromagnetic response is primarily sensitive to the distance between the instrument and the ice–ocean interface (Thomas, 2025).

Haas et al. (1997) showed that it is possible to derive under-pond SIT from *GEM* measurements on top of melt ponds. Here we use literature values (Thomas, 2025; Haas et al., 1997) to assume the conductivity of the sea ice plus snow layer as 0.05 S m^{-1} and the conductivity of sea water as 2.55 S m^{-1} for all measurements, including the calibrations. Further, we assume that melt pond water has the same conductivity as the sea ice and snow layer (0.05 S m^{-1}). Based on this assumption we can derive the under-pond SIT from *GEM* measurements within melt ponds after subtracting the measured melt pond depth. A comparison of five *GEM*-derived under-pond SIT estimates with co-located drilling measurements (melt pond depth was subtracted from the *GEM* draft estimates to obtain under-pond SIT) within the same melt pond showed a bias of -0.04 m, MAE of 0.15 m and RMSE of 0.19 m for the under-pond SIT (see Tab. A1 in Appendix). Nonetheless, it should be noted that, for level ice, the *GEM* measurements have large horizontal footprints of about 4 times the sea ice thickness (Itkin et al., 2023; Reid and Vrbancich, 2004). Accordingly, the *GEM* measurements cover a much a wider surface area compared to the point measurements of the drillings. The *GEM* measurements were calibrated using the *EMPEX* (empirical exponential) approach (Pfaffling et al., 2007) at each floe visit during the expedition by placing the *GEM* instrument on different known heights above level sea ice surface using a wooden ladder. Directly below the ladder the SIT was measured at five drill holes. These calibration measurements provide an exponential relationship between the complex EM response and the SIT. For the melt pond measurements the *GEM* instrument was placed within a Pulka sledge, with a height-offset of about 0.02 m to the water level, on the melt pond water surface to measure the sea ice draft within the image area for a few seconds. Afterwards the averaged melt pond depth corresponding to this image is subtracted from the measured sea ice draft to get the under-pond SIT. We use the 18325 Hz in-phase channel to retrieve the under-pond SIT as it has the highest signal-to-noise ratio and was also used for this reason during the *MOSAiC* expedition (Itkin et al., 2023).

Figure 4 shows the distributions of melt pond depth and under-pond SIT for all 67 co-located hyperspectral images. Under-pond SIT ranges from 0.17 to 2.83 m, covering most of the current Arctic level sea ice thickness range, excluding ridges (Thomas (2025), Figure 1.12; Webster et al. (2026)). Of these measurements, 49 were obtained by drilling and 18 using the *GEM* instrument. Melt pond depths likewise cover the typical range observed on first-year and multiyear ice (Morassutti and Ledrew, 1996). All under-pond SIT and melt pond depth measurements are published by Clemens-Sewall et al. (2026, in

https://doi.org/10.5194/egusphere-2026-7079
Preprint. Discussion started: 24 November 2026
© Author(s) 2026. CC BY 4.0 License.

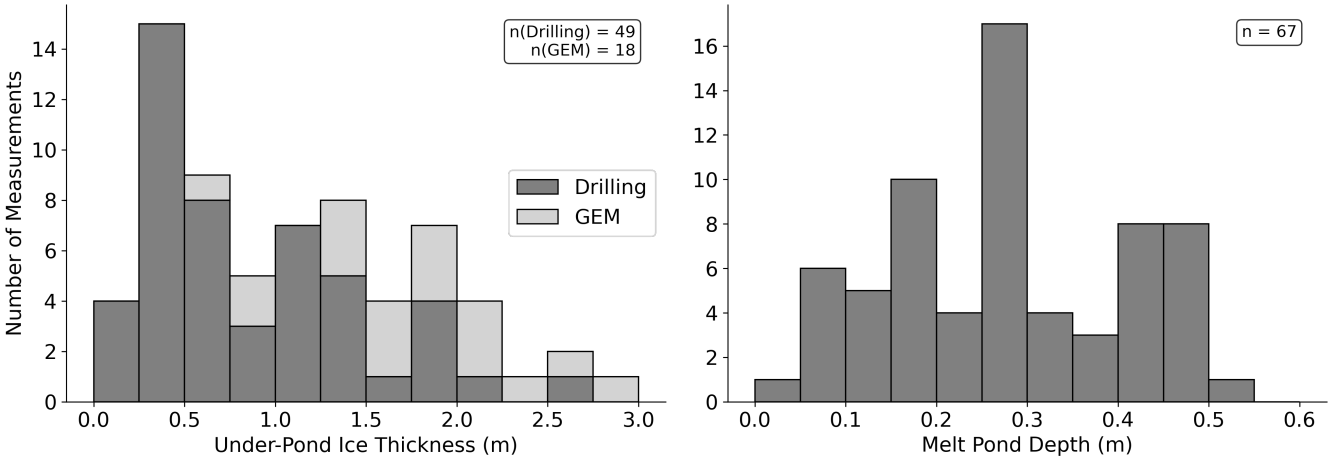

Figure 4. The first histogram (a) shows the distribution of all co-located under-pond SIT measurements for the analyzed dataset of 67 hyperspectral images. It is a stacked histogram, meaning the histograms of GEM- and drill-measured values are stacked on top of each other and do not overlap. The second histogram (b) shows the distribution of co-located melt pond depth measurements.

prep., see data availability section for the archiving status). Compared with previous datasets of co-located spectral albedo and under-pond SIT measurements (Table 1), this dataset is considerably larger and covers a broader range of ice thicknesses and pond-bottom conditions. It therefore provides an extensive observational basis for investigating the reflectance–SIT relationship and its dependence on pond-bottom structure.

2.2 Simulated melt pond reflectance

To assess whether radiative transfer theory reproduces the observed relationship between spectral melt pond reflectance and under-pond SIT, we use the melt pond reflectance model of Malinka et al. (2018). These simulations allow us to vary ice thickness, and ice scattering properties independently, helping to distinguish their individual effects on reflectance. In particular, we investigate whether differences between homogeneous and bubbly pond bottoms can be explained by variations in the transport scattering coefficient. Comparing simulated and measured reflectance thus provides a physical basis for interpreting the observed relationships and assessing their implications for under-pond SIT retrievals. In the following we give a brief overview of the Malinka et al. (2018) model and our model set-up.

The forward model conceptualizes a melt pond as a plane-parallel layer of pure meltwater (i.e., freshwater) overlying a layer of sea ice, which serves as the pond bottom. Under this framework, light attenuation within the water layer follows an exponential law, assuming Rayleigh scattering is negligible relative to water absorption. The pond bottom is assumed to be a Lambertian reflector, reflecting light isotropically. Total reflectance is calculated as the sum of Fresnel reflection at the water surface and multiple internal reflections between the water surface and the melt pond bottom. The spectral albedo of the pond

https://doi.org/10.5194/egusphere-2026-7079
Preprint. Discussion started: 24 November 2026
© Author(s) 2026. CC BY 4.0 License.

Table 1. All datasets of co-located melt pond spectral albedo and under-pond sea ice thickness measurements. This table is an adapted version of Table 1 in Zhang et al. (2022)

Source	Location	Time of measurements	Nr. of measure-ments	Under-pond SIT range	Wave-length range	Sky conditions
Perovich (1998)	Near 71°N, 156°W	9 June 1995	1	1.6 m	400–1000 nm	Clear sky
Perovich et al. (2002) & Malinka et al. (2018)	75°N–80°N, 142°W–162°W	June–August 1998	8	0–1.2 m	400–1000 nm	Overcast sky
Light et al. (2015)	67°N–75°N, 150°W–175°W	June 2010 & July 2011	24	0.49–1.5 m	350–1300 nm	Clear and overcast sky
Istomina et al. (2016)	84°N–82°N, 31°E–129°E	August 2012	17	0.4–3.0 m	350–1300 nm	Clear and overcast sky
Cao et al. (2020)	79°N–85°N, 156°W–170°W	August 2018	5	1.0–1.5 m	350–920 nm	Overcast sky
Ringel et al. (2026)	82°N–85°N, 34°W–18°E	July–August 2025	67	0.2-2.8 m	400–900 nm	Clear and overcast sky

bottom is derived using a two-stream approximation and depends on the transport optical thickness, $\tau_t = (\sigma_t + \alpha_i)H_i$, through an exponential term. σ_t is the transport scattering coefficient α_i the absorption coefficient and H_i the under-pond SIT. This allows determination of the reflective properties of the pond, including its bidirectional reflectance factor and albedo under direct or diffuse incidence. The model is parameterized by three independent scalar variables: the pond depth (z), the underlying ice thickness (H), and the transport scattering coefficient of the ice (σ_t). The transport scattering coefficient σ_t relates to the scattering coefficient σ through the asymmetry parameter g via $\sigma_t = \sigma(1-g)$, where g represents the mean cosine of all scattering angles within the scattering media. For strongly forward-scattering media such as sea ice, σ_t provides a more physically meaningful measure of radiative transfer than σ alone, as it accounts for the reduced effective scattering when photons are predominantly scattered in the forward direction (Malinka et al., 2018). Investigations into the inherent optical properties (IOPs) of sea-ice constituents, such as brine inclusions and air bubbles, conclude that σ_t is spectrally neutral across visible and near infrared wavelengths (Malinka et al., 2018). Consequently, the spectral character of the pond reflectance is primarily determined by the known absorption coefficients of water and solid ice.

Table 2 lists all parameters and their assumed values of our simulations. Only under-pond SIT and σ_t are varied in the model to simulate the relationship of melt pond reflectance and under-pond SIT for the different melt pond bottom types. We assign high σ_t values (3.6–6.0 m^{-1}) to represent bubbly bottoms, low values (0.3–1.8 m^{-1}) for homogeneous bottoms, and

https://doi.org/10.5194/egusphere-2026-7079
Preprint. Discussion started: 24 November 2026
© Author(s) 2026. CC BY 4.0 License.

Table 2. All parameters used in the simulations with the model of Malinka et al. (2018). If only a single value is given, the parameter was fixed for all simulations. Only for the varied parameters under-pond sea ice thickness (SIT) and transport scattering coefficient σ_t multiple values are shown. The value for the under-pond SIT is varied by increments of 0.2 m.

Parameter	Value(s)
Melt pond fraction	$100\,\%$
Open water fraction	$0\,\%$
Melt pond depth	$0.2\,\mathrm{m}$
Absorption coefficient at $390\,\mathrm{nm}$	$0.3\,\mathrm{m}^{-1}$ (Zege et al., 2015)
Effective grain size	$3.333\,\mathrm{mm}$ (Zege et al., 2015)
Optical thickness of sea ice	8.5 (Zege et al., 2015)
Relative azimuth angle	$23°$
Observational zenith angle	$0°$
Solar zenith angle	$60°$
Under-pond SIT	$0.2, 0.4, \ldots, 3.0\,\mathrm{m}$
σ_t (homogeneous bottom)	$0.3, 0.6, 1.2, 1.8\,\mathrm{m}^{-1}$
σ_t (non-selective bottom)	$1.2, 2.4, 3.6, 4.8, 6.0\,\mathrm{m}^{-1}$
σ_t (bubbly bottom)	$3.6, 4.8, 6.0\,\mathrm{m}^{-1}$

intermediate to high values (1.2–6.0 m^{-1}) for the non-selective bottoms. Assuming $g = 0.94$ the total range of our assumed σ_t values (0.3–6.0 m^{-1}) translates to a range of 5 m^{-1} to 100 m^{-1} of σ values. A realistic range for σ_t of sea ice is 0.1 m^{-1} to 10 m^{-1} according to Malinka et al. (2018) and Mobley et al. (1998), i.e., our simulations roughly cover that realistic range. The under-pond SIT is varied from 0.2 m to 3.0 m in increments of 0.2 m, which corresponds to the SIT range observed during *CONTRASTS* (Fig. 4). The resulting simulations are discussed alongside the observations in Sec. 3.1.1.

2.3 Conversion of hyperspectral reflectance spectra to RGB and YIQ colors

To convert the hyperspectral reflectance measurements (Sec. 2.1.2) into RGB values for visualization and statistical analysis in Sec. 3.2, we adopt the colorimetric conversion approach of Lu et al. (2018).The aim of this colorimetric conversion method is less about reproducing human-perceived melt pond colors than about using a standardized conversion method which is also used for common RGB cameras. Instead of reiterating the detailed calculations for this conversion here we refer to the corresponding equations presented in Lu et al. (2018). Here we give a brief overview about the three major processing steps and our adjustments:

1. Each reflectance spectrum (α_λ in Lu et al. (2018)) is first weighted by the spectra of the D65 illuminant - the standard daylight illuminant defined by the International Commission on Illumination (CIE). Lu et al. (2018) used a measured spectrum of Grenfell and Perovich (2008) taken during an overcast day (August 7, 2005) on Arctic sea ice as the illuminant ($F_0(\lambda)$ in Lu et al. (2018)). We decided to use the CIE standard daylight illuminant D65 which is defined for

https://doi.org/10.5194/egusphere-2026-7079
Preprint. Discussion started: 24 November 2026
© Author(s) 2026. CC BY 4.0 License.

mid-latitude daylight conditions. Although this choice does not allow for a perfectly accurate representation of human-perceived melt pond colors in the Arctic it makes our results in Sec. 4 more transferrable to images of common RGB cameras as the D65 illuminant is also used for the widely used AdobeRGB color space.

2. The illuminant-weighted reflectance spectrum ($\alpha_\lambda \cdot F_0(\lambda)$) is then integrated against the CIE 1931 2° standard observer color-matching functions $\bar{x}(\lambda)$, $\bar{y}(\lambda)$, $\bar{z}(\lambda)$ to obtain CIE XYZ tristimulus values (see Eq. 2 in Lu et al. (2018)). These color-matching functions are internationally standardized functions to describe the spectral sensitivity of the average human observer. For the D65 illuminant and the color matching functions we used the definitions provided by the Python package `colour` (Colour Developers, 2025).

3. The tristimulus XYZ values are subsequently transformed into linear RGB using the Adobe RGB (1998) primaries ((x_r, y_r)=(0.640, 0.330), (x_g, y_g)=(0.210, 0.710), (x_b, y_b)=(0.150, 0.060) and the D65 white point ((x_w, y_w)=(0.313, 0.329)) (see Eq. 3-6 in Lu et al. (2018)).

Because most consumer RGB cameras use AdobeRGB and are likewise designed and calibrated to approximate the CIE 1931 color-matching functions (typically via Bayer-filter spectral sensitivities tuned to match human vision), this colorimetric conversion method makes our results more comparable to those that would be recorded by a conventional RGB camera photographing the same melt ponds under the same daylight illumination. However, we do not apply any gamma correction or encoding and keep the linear RGB values for all further processing unless otherwise stated. Accordingly, image data from other common RGB cameras has to be linearized in this regard before they are radiometrically comparable to our results. It should be noted here, that the general relationship of pond reflectance and under-pond SIT shown in Sect. 3 as well as the retrieval fits shown in Sect. 4 do not change significantly when changing the color conversion method from the CIE colorimetric approach to more simple gaussian-shaped RGB response functions (not shown).

In Sect. 3.2.2 we also explore the potential of the YIQ (Y=Luma, I=In-phase, Q=Quadrature) color space for an under-pond SIT retrieval. The conversion from linear RGB to YIQ color is performed using the Python standard-library module `colorsys` (Python Software Foundation, 2025). This conversion applies a fixed linear 3×3 matrix on the RGB vector (Y = 0.3000 R + 0.5900G + 0.1100B, I = 0.5990R - 0.2773G - 0.3217B, Q = 0.2130R - 0.5251G + 0.3121B), with no gamma correction.

3 How optical melt pond observations relate to under-pond SIT

This section presents and discusses our hyperspectral melt pond measurements and their relationship to under-pond SIT. Section 3.1 examines spectral differences between bubbly and homogeneous pond bottoms, evaluates their representation in a numerical reflectance model, and assesses whether the two types can be distinguished from hyperspectral measurements. Section 3.2 explores the relationship between melt pond color and under-pond SIT using different color spaces.

https://doi.org/10.5194/egusphere-2026-7079
Preprint. Discussion started: 24 November 2026
© Author(s) 2026. CC BY 4.0 License.

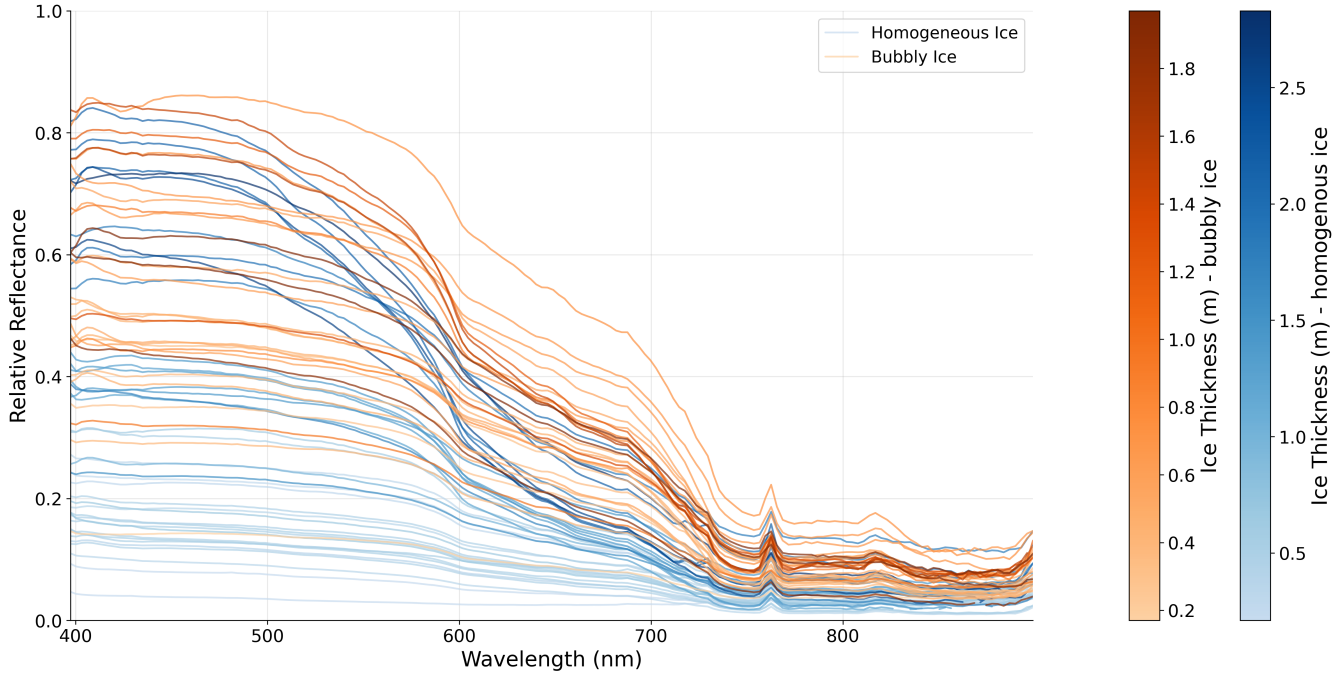

Figure 5. All measured reflectance spectra for the homogeneous (blue shaded lines) and bubbly (orange shaded lines) pond bottoms. The respective blue and orange shading indicates the respective SIT. Note the different scales of the two SIT color bars.

3.1 Melt pond reflectance

Figure 5 shows the measured reflectance spectra of all homogeneous and bubbly melt pond bottom cases separated by different color coding. To start with, all measured spectra exhibit the typical shape of melt pond reflectance (high reflectance at short wavelengths, low reflectance at long wavelengths) as well as the distinct oxygen peak described earlier. Further, the color-coding visualizes the increase in reflectance with increasing under-pond SIT, especially for the spectral range of 400-600 nm. By comparing the two categories of spectra separated by the pond bottom type, it becomes clear that the reflectance spectra of bubbly pond bottoms (orange lines in Fig. 5) are generally shifted towards higher reflectances across the whole spectrum. That is despite the fact that their range of under-pond SIT is smaller than the range of the homogeneous pond bottom SIT (note the different scales of the color bars in Fig. 5). Even in the NIR range the reflectance of bubbly pond bottoms is slightly higher than that of homogeneous pond bottoms. The differences between the two categories of pond bottoms are not limited to absolute reflectance values. The spectral shapes of reflectance also appear to differ systematically in certain spectral ranges: Most of the reflectance spectra of bubbly melt pond bottoms have less pronounced negative slopes especially at 500–600 nm but also at 600–700 nm. This systematic difference in spectral shape between both melt pond bottom types will be analyzed and discussed in more detail in Sec. 3.1.2.

To visualize the relationship between melt pond reflectance and under-pond SIT more directly, Fig. 6 plots all 67 reflectance

https://doi.org/10.5194/egusphere-2026-7079
Preprint. Discussion started: 24 November 2026
© Author(s) 2026. CC BY 4.0 License.

measurements against co-located under-pond SIT. Panels a), b), and c) show the non-selective, homogeneous, and bubbly pond-bottom datasets, respectively. The wavelengths 400 nm, 600 nm, and 800 nm represent the characteristic spectral regions described above. The dashed lines show least-squares fits. We use a logarithmic function, $R = a + b\ln(H_i)$, for the non-selective and bubbly datasets and a linear function, $R = a + b\,H_i$, for homogeneous bottoms. Here, R is relative reflectance and H_i is under-pond SIT. For homogeneous bottoms, we also compare the linear fit with a logarithmic fit. Tab. A2 in the Appendix lists all fit functions and their coefficients of determination (R^2).

In the non-selective dataset (Fig. 6, left panel), reflectance at 400 nm and 600 nm increases strongly with under-pond SIT, as it does in the other two datasets (middle and right panel). At 800 nm, none of the three datasets shows a significant SIT dependence, as expected due to the increased water absorption at this wavelength. The logarithmic fits for the non-selective measurements yield R^2 values of 0.54 at 400 nm and 0.38 at 600 nm (Tab. A2). Above 1 m, reflectance continues to increase at 400 nm and levels off near 0.4 at 600 nm. The steep rise over thinner ice and the saturation at 600 nm are consistent with previous studies showing that melt pond albedo increases nonlinearly with under-pond SIT before approaching an asymptote (Zege et al., 2015; Lu et al., 2016, 2018; Malinka et al., 2018; Zhang et al., 2021).

For bubbly pond bottoms (Fig. 6, right panel), the logarithmic fits yield R^2 values of 0.33 at 400 nm and 0.23 at 600 nm (Tab. A2). Reflectance rises particularly steeply below 1 m. Up to 1.5 m, bubbly bottoms are approximately twice as reflective as homogeneous bottoms (Fig. 6, middle panel). Above 1 m, reflectance at 400 nm varies between 0.6 and 0.8, while reflectance at 600 nm levels off near 0.4.

Homogeneous pond bottoms (Fig. 6, middle panel) in contrast, show a near-linear increase in reflectance with SIT. At 400 nm and 600 nm, there is no clear evidence of saturation over the observed range (0–3 m). The linear fits explain 85 % and 79 % of the variance, respectively, compared with 76 % and 74 % for the logarithmic fits (Tab. A2). The corresponding linear slopes are 0.26 m^{-1} and 0.13 m^{-1}. To our knowledge, previous studies did not report such a linear dependence for melt pond reflectance. We describe it as near-linear because the fits are based on few data points.

The analyzed contrast between bubbly and homogeneous pond bottoms underlines that air bubbles systematically affect how reflectance varies with under-pond SIT. The combination of the two bottom types in the non-selective dataset obscures the near-linear relationship for homogeneous melt pond bottoms.

Substantial reflectance variability remains around the fitted relationships in all three datasets. The marker styles in Fig. 6 show no clear association with sky conditions. Relative azimuth and sun elevation angles also do not explain the variability (see Appendix Figs. B1 and B2). We assume that the remaining variability is primarily due to differences in pond-bottom IOPs driven by air-bubble microstructure.

https://doi.org/10.5194/egusphere-2026-7079
Preprint. Discussion started: 24 November 2026
© Author(s) 2026. CC BY 4.0 License.

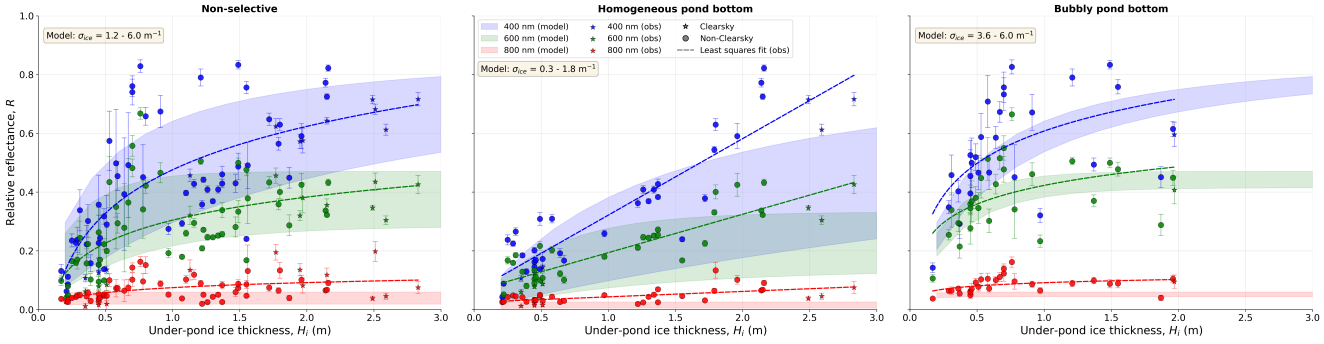

Figure 6. Observations and simulations of spectral melt pond reflectance versus under-pond sea ice thickness. The marker show the measured reflectances (Sect. 2.1.2) at specific wavelengths, 400 nm, 600 nm and 800 nm, against the co-located under-pond SIT measurements (Sect. 2.1.3) for non-selective (left panel), homogeneous (middle panel) and bubbly (right panel) pond bottoms. These spectral measurements represent spatial averages over manually selected image areas as shown in Fig. 2. The error bars of the markers show the standard deviation within the area over which the spectral reflectance was averaged. The different marker types (star, circle) indicate clear sky or non-clear sky conditions during the respective measurement. The dashed lines are the least squares fits to the observations which are presented in detail in Tab. A2. The color-shadings show the range of simulated melt pond reflectances (Sect. 2.2 & 3.1.1) using the model of Malinka et al. (2018). The value-ranges used for the transport scattering coefficient σ_t of the simulations for the three types of pond bottom are given in the upper left box.

We also investigated how our hyperspectral melt pond reflectance measurements relate to melt pond depth, using the same analysis methods, but did not find any clear relationship (not shown).

3.1.1 Numerical simulations of melt pond bottom reflectance

To test whether realistic variations in σ can reproduce the observed reflectance-SIT relationships and variability for the three pond bottom types we use the simulations described in Sec. 2.2.

For non-selective and bubbly pond bottoms, the simulated reflectances (color shading in Fig. 6) increase logarithmically with under-pond SIT. At 400 nm and 600 nm, both the curvature and the absolute reflectance values agree closely with the least-squares fits to the observations (left and right panels, respectively).

For homogeneous pond bottoms, the simulations approach a more linear dependence as σ_t decreases. However, the analytical formulation of Malinka et al. (2018) (Sect. 2.2) cannot reproduce the observed near-linear relationship, even at very low σ_t. Especially above 1.5 m under-pond SIT simulated reflectances are substantially lower than observed at all three wavelengths. This systematic discrepancy between a well established melt pond reflectance model and observations indicates that previous model studies did not account for a linear dependence of melt pond reflectance on under-pond SIT as we observe it here.

https://doi.org/10.5194/egusphere-2026-7079
Preprint. Discussion started: 24 November 2026
© Author(s) 2026. CC BY 4.0 License.

The range of σ_t values used in the simulations captures most of the observed reflectance variability in the non-selective dataset. This further supports our assumption and previous literature results that air-bubble microstructure primarily drives variability in melt pond reflectance. For bubbly bottoms, however, the simulated range is narrower than observed. For homogeneous bottoms, the simulated range is comparable to the observed range at 600 nm and too wide at 400 nm.

3.1.2 Discriminating different melt pond bottom types from reflectance

The previous subsections demonstrated that melt pond bottoms containing air bubbles have a systematically different and more complex physical relationship to reflectance than homogeneous melt pond bottoms. We based this analysis on a visual categorization on reflectance measurements into bubbly and homogeneous melt pond bottoms. But is it possible to automatically discriminate between those two melt pond bottom types based on their hyperspectral fingerprints? Such a melt pond bottom type discrimination would allow an under-pond SIT retrieval to take the two fundamentally different relationships into account, making it more precise.

Absolute reflectance at specific wavelengths, as presented in the previous section, cannot reliably distinguish between the two melt pond bottom types, as both can exhibit similar reflectance values at the same under-pond SIT (Fig. 6). However, as already mentioned in Sect. 1 and visible in Fig. 5 the measured reflectance spectra of both melt pond bottom types do have one consistent difference: The spectral slope. In the following we investigate whether the spectral slope of melt pond reflectance spectra can be used to discriminate between homogeneous and bubbly melt pond bottoms.

In a first step we identify spectral regions in which the spectral slopes of both pond bottom types differ by taking the first derivative of all reflectance spectra the following way for the whole observed spectrum:

$$S_{\lambda_i} = \frac{R_{\lambda_i} - R_{\lambda_{i-1}}}{\lambda_i - \lambda_{i-1}}, \tag{1}$$

where S_{λ_i} is the slope value at wavelength λ_i and R_{λ_i} the spectral reflectance at wavelength λ_i. This analysis shows that the differences in reflectance slope between the two pond bottom types are particularly pronounced in the 690–730 nm range compared with the rest of the observed spectrum (not shown). Figure 7 zooms into this specific spectral range and shows that in most cases the reflectance spectra of bubbly melt pond bottoms have steeper slopes than the reflectance spectra of homogeneous melt pond bottoms. Based on this result, we conclude that deriving the slope of a melt pond reflectance spectrum within 690–730 nm offers a simple but effective possibility to differentiate between bubbly and homogeneous melt pond bottoms.

In a second step we therefore derive the mean reflectance slope between 690 and 730 nm for each reflectance spectra. The slope is determined as the gradient of an ordinary least-squares linear regression fitted to all spectral reflectance measurements within this wavelength range (approximately 14 for the *Specim IQ*'s spectral sampling):

$$\bar{S} = \frac{\sum_{i=1}^{N} \left(\lambda_i - \bar{\lambda}\right)\left(R_i - \bar{R}\right)}{\sum_{i=1}^{N} \left(\lambda_i - \bar{\lambda}\right)^2}, \qquad 690\,\mathrm{nm} \leq \lambda_i \leq 730\,\mathrm{nm} \tag{2}$$

https://doi.org/10.5194/egusphere-2026-7079
Preprint. Discussion started: 24 November 2026
© Author(s) 2026. CC BY 4.0 License.

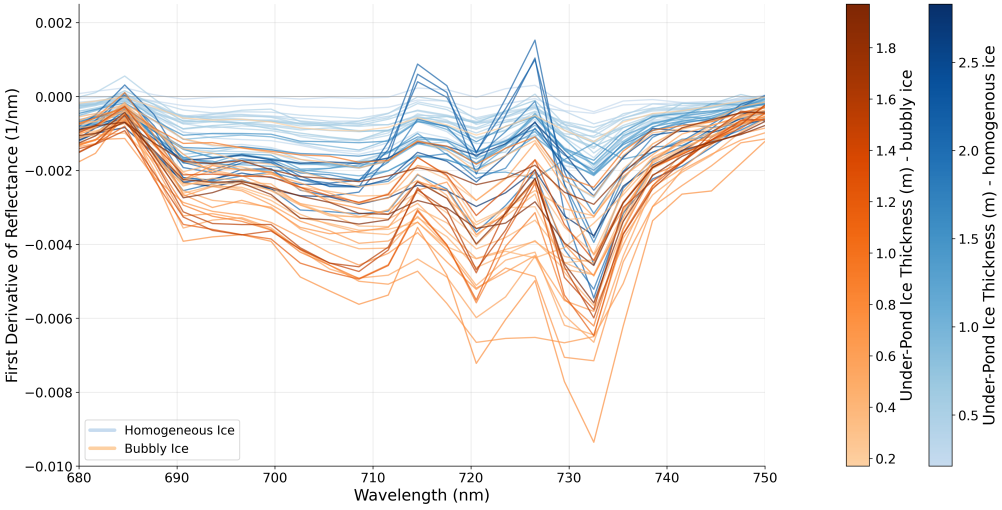

Figure 7. The first derivatives of the reflectance spectra shown in Fig. 5 for the spectral range of 680-750 nm calculated using Equation 1. As in Fig. 5 the blue and orange color shading refers to homogeneous and bubbly pond bottom ice thickness, respectively.

where $\bar{S}$ is the mean reflectance slope (nm^{-1}), R_i is the reflectance at wavelength λ_i, N is the number of spectral bands within the range, and $\bar{\lambda}$ and $\bar{R}$ are the mean wavelength and mean reflectance of those bands. The calculated slope values $\bar{S}$ for all 67 measured spectra, color-coded by the respective pond bottom type, are shown in Fig. 8. The figure shows that most bubbly reflectance spectra have a spectral slope less than about -0.002 nm^{-1} while most slope values of the homogeneous spectra are above. We select a spectral-slope threshold separating bubbly and homogeneous reference spectra by maximizing Youden's index J (Youden (1950), $J = \mathrm{True\ Positive\ Rate} + \mathrm{True\ Negative\ Rate} - 1$). A J value of -1 would mean only false classifications, 0 no classification skill and 1 perfect classification skill. This method yields a threshold value for our dataset of -0.0021 nm^{-1} ($J = 0.844$), with 90% of bubbly spectra correctly classified as bubbly ($\mathrm{True\ Positive\ Rate}$) and 95% of homogeneous spectra correctly classified as homogeneous ($\mathrm{True\ Negative\ Rate}$) (Fig. 8). Based on this and considering the low number of 67 spectra we recommend to use a slope value of $-0.002\,\mathrm{nm}^{-1}$ as a reasonable threshold to discriminate bubbly from homogeneous melt pond bottoms.

In a third step we apply this method and threshold to the two hyperspectral images already shown in Fig. 3. These two images are a useful test case as we already know, based on the analysis of the corresponding ice cores, that one bottom contains air bubbles and the other does not contain any air bubbles. The results show that the spectral slope criterion correctly identifies the bright areas within the melt pond of Fig. 9 (left) as bubbly pond bottom. And for the homogeneous melt pond bottom of Fig. 9 (right) - correctly - no pixel is identified as bubbly melt pond bottom. We provide some more test cases of this method for other hyperspectral images in Fig. B3 in the Appendix. Applying this method to every single image from our dataset gives an average fraction of around 29% of pixels with bubbly pond bottom.

https://doi.org/10.5194/egusphere-2026-7079
Preprint. Discussion started: 24 November 2026
© Author(s) 2026. CC BY 4.0 License.

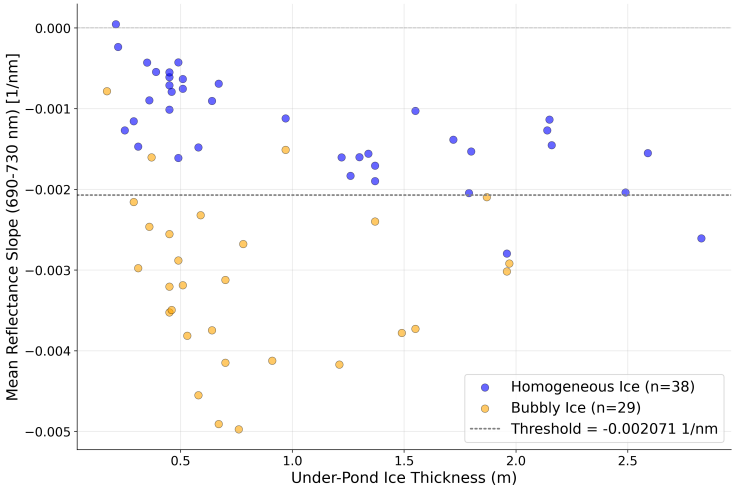

Figure 8. All mean reflectance slope ($\bar{S}$) values calculated using Eq. 2 for the spectral range 690–730 nm are shown for the measurements with only bubbly or homogeneous melt pond bottoms. The color-coding indicates the corresponding melt pond bottom. The dashed line shows the threshold value of -0.0021 nm^{-1}. This threshold could be used to automatically categorize measurements into homogeneous pond bottom (above threshold) and bubbly pond bottom (below threshold).

The analysis of this subsection shows that it is indeed possible to automatically discriminate bubbly from homogeneous melt pond bottoms based on their different spectral slopes within 690-730 nm. The method described here could be used to discriminate between bubbly and homogeneous melt pond bottoms before retrieving under-pond SIT. The value of such a pond bottom type retrieval will be demonstrated in Sect. 4.

3.2 Melt pond color

3.2.1 RGB color space

The previous section shows that the reflectance information most relevant to under-pond SIT is concentrated in three spectral regions that roughly correspond to the blue, green, and red portions of the visible spectrum. A principal component analysis of the full measured spectrum yielded a similar result (not shown). This motivates a systematic investigation of whether color-based parameter derived from standard RGB imagery – rather than full hyperspectral data – can serve as robust predictors of under-pond SIT. This would enable under-pond SIT retrieval algorithms applicable to more common RGB-capable drone, airborne, and satellite sensors. For this analysis we convert all hyperspectral measurements (Sec. 2.1.2) to RGB values via the colorimetric method described in Sec. 2.3.

https://doi.org/10.5194/egusphere-2026-7079
Preprint. Discussion started: 24 November 2026
© Author(s) 2026. CC BY 4.0 License.

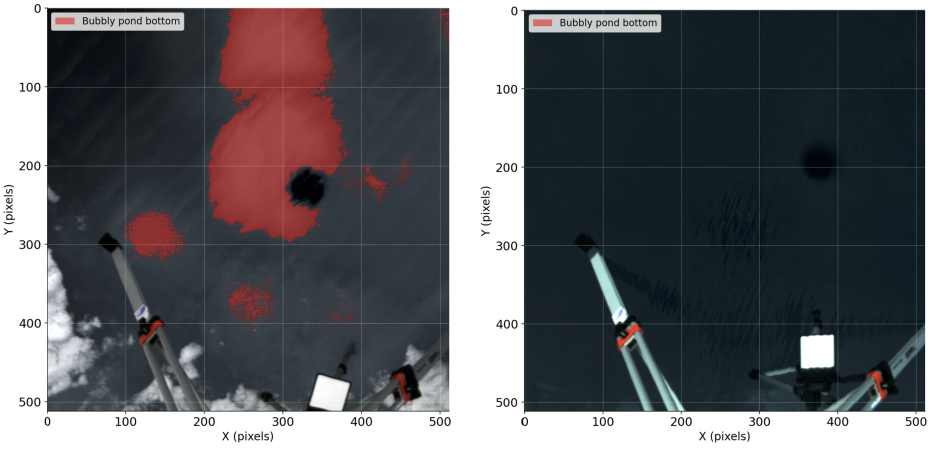

Figure 9. Both images show RGB composites of the same hyperspectral images shown in Fig. 3 (*PS149_2025-07-30_021 & PS149_2025-07-30_023*). The red area shows pixels which have an average spectral slope value $\bar{S}$ within 690–730 nm below -0.002 nm^{-1}. These pixels are therefore categorized as "bubbly" pond bottom. If no color is shown the pond bottom is categorized into "homogeneous" pond bottom.

Figure 10 shows the average RGB melt pond colors against 0.5 m bins of under-pond SIT. The hyperspectral reflectances are converted to linear RGB values first and then these linear RGB values are averaged for each 0.5 m bin. Accordingly, each bin represents the average RGB color for the corresponding range of under-pond SIT. It should be noted here again that the displayed RGB colors of Fig. 10 are not meant to perfectly reproduce human-perceived melt pond colors. This is why we also do not apply any gamma correction here. Instead this analysis focuses on the qualitative shift in color brightness and chromaticity as well as the contrasts between homogeneous and bubbly pond bottom colors.

The overall tendency towards brighter, bluer colors with increasing under-pond SIT is visible under both non-clear sky and clear-sky conditions. The smoothest color gradient is observed for homogeneous pond bottoms under non-clear sky conditions, indicating the strongest and most systematic color–SIT relationship. For bubbly pond bottoms the gradient is less regular, as thin ice below 1 m already produces bright blue colors owing to the enhanced light scattering by the enclosed air bubbles discussed in the previous Sections. This results in brighter melt pond colors than the colors of homogeneous melt pond bottoms having the same under-pond SIT.

3.2.2 YIQ color space

Although, RGB color shows correlation to the under-pond SIT as shown in the previous section, it is not the best choice as a predictor for it. The disadvantage of RGB is that all three channels are strongly correlated as they mainly respond to the same underlying physical quantity – total reflected radiance. The results of Sec. 3.1.1 and 3.2.1, however, prove that the under-pond SIT affects both, the melt pond reflectance (brightness) as well as the melt pond color (chromaticity). Consequently, a retrieval for under-pond SIT should be based on a color space which is defined on dimensions that separate these two physical quanti-

https://doi.org/10.5194/egusphere-2026-7079
Preprint. Discussion started: 24 November 2026
© Author(s) 2026. CC BY 4.0 License.

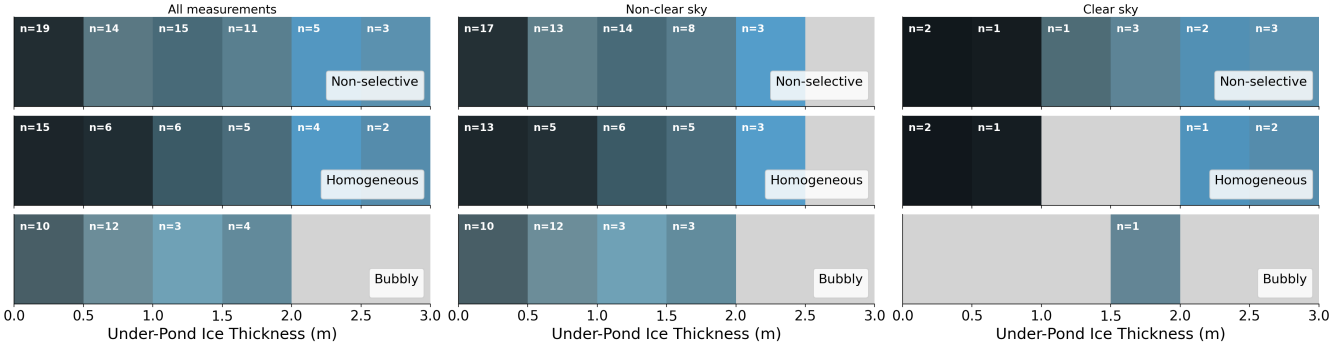

Figure 10. Average RGB melt pond colors for 0.5 m bins of under-pond SIT. The RGB colors within each rectangle show the average (linear) RGB color derived from the hyperspectral measurements within each 0.5 m bin of under-pond SIT for different illumination conditions (left: all measurements, middle: non-clear sky, right: clear sky). Each subplot shows this for the non-selective dataset (upper panel), the homogeneous-bottom sub-dataset (middle panel), and the bubbly-bottom (lower panel). The numbers n in the upper left parts of the colored rectangles indicate how many measurements are within each bin. Grey areas indicate no data.

ties. The YIQ color space is doing this by separating the luminance (Y) from the two chrominance components (I and Q) that encode color differences along orange–cyan and green–magenta axes, respectively. To verify whether this makes the YIQ color space a better choice for an under-pond SIT retrieval we convert the RGB values to YIQ values (Sect. 2.3) and compare the correlations of the individual color space parameters Y, I and Q with under-pond SIT for our measurements. We also did this analysis using other color spaces such as HSL (Hue-Saturation-Lightness) but the YIQ color space performed best regarding individual channel correlations with under-pond SIT and complementary information (brightness and chromaticity). Therefore, we only present the analysis results based on the YIQ color space.

The three YIQ color space parameters are plotted against the corresponding co-located under-pond SIT for each pond bottom type in Fig. 11. We show the Spearman rank correlation ρ between the color space parameter and the under-pond SIT in each figure panel. The Spearman rank correlation is used instead of the Pearson correlation coefficient r as it is more robust to outliers and better suited to capture non-linear relationships. Additionally, we either add a linear or logarithmic fit to each panel. The function of the fit (logarithmic or linear) is decided on the higher R^2 value of both and only serves to demonstrate which function is more suited to describe the observed dependence. The same kind of scatter plots for the RGB and HSL color space components can be found in the Appendix (Fig. B4 & B5).

The Luma parameter Y (Fig. 11, a-c) is positively correlated with under-pond SIT. Further, the same general dependence on under-pond SIT as for spectral reflectance is visible: Linear increase for the homogeneous pond bottom cases (Fig. 11b) with a Spearman rank correlation of $\rho = +0.85$ and logarithmic increase for the bubbly pond bottom cases (Fig. 11c) with $\rho = +0.54$. The non-selective measurements show a mixture of both pond bottom signals (Fig. 11a), therefore, also a logarithmic increase with $\rho = +0.70$. This overall similarity to the spectral reflectances shown in Sec. 3.1 is expected as Y represents the brightness,

https://doi.org/10.5194/egusphere-2026-7079
Preprint. Discussion started: 24 November 2026
© Author(s) 2026. CC BY 4.0 License.

thus relates directly to the total reflected radiance of the melt pond.

The in-phase parameter I (Fig. 11, d-f) - representing the orange–cyan axis of the chromaticity - is negatively correlated to under-pond SIT. As a decrease in in-phase I means a shift to more blueish colors, this negative correlation corresponds to the general color dependency also seen in the RGB colors of Fig. 10. Therefore, it is also not surprising that the negative correlation is linear for homogeneous melt pond bottoms with $\rho = -0.85$. The non-selective pond bottom measurements also show a clear overall linear and negative response of the in-phase parameter I to an increase in under-pond SIT ($\rho = -0.83$). This underlines the mentioned general shift towards blue color (Fig. 11d). Despite this overall linear dependency for non-selective bottoms, the in-phase parameter shows a more logarithmic-shaped dependence on under-pond SIT for bubbly melt pond bottoms ($\rho = -0.67$).

As the Quadrature parameter Q (Fig. 11, g-i) represents the green–magenta axis of the chromaticity it represents colors which are less dominant in melt ponds. Consequently, the correlations of Q and under-pond SIT are much lower than for I. However, with $\rho = -0.41$, $\rho = -0.56$ and $\rho = -0.47$ for the non-selective, homogeneous and bubbly melt pond bottoms, respectively, the Quadrature component is also negatively correlated with under-pond SIT. All parameter have a logarithmic dependence on under-pond SIT.

Figure 11 shows that bubbly melt pond bottoms tend to have an overall brighter appearance than homogeneous melt pond bottoms. For thin melt pond bottoms below 1 m under-pond SIT, bubbly melt pond bottoms reach up to twice as high luminance values (Fig. 11c) as the homogeneous melt pond bottoms (Fig. 11b). Only for thicker melt pond bottoms close to 2 m under-pond SIT and above, the measurements indicate that the luminance of both melt pond bottom types is in a similar range. Apart from this luminosity difference, the in-phase and quadrature values also indicate a small but systematic difference of chromaticity between the two pond bottom types. Both the in-phase and quadrature components tend to be lower for bubbly melt pond bottoms across the observed range (0-2 m). Further, the YIQ color space parameters do not systematically depend on the sky conditions (e.g., clear sky, non-clear sky) as indicated by the color coded scatter markers in Fig.12.

In summary, the YIQ color space shows strong correlations between its individual parameters, especially the luma Y and in-phase I parameters, and under-pond SIT. It also shows a color difference between bubbly and homogeneous melt pond bottoms and indicates that bubbly melt pond bottoms have significantly higher luminosity (brightness) for under-pond SIT below 2 m. This means common RGB images do contain the physical information relevant to retrieve under-pond SIT. Based on this result, we develop an empirical under-pond SIT retrieval in the following section.

4 Empirical ground-based under-pond SIT retrieval

The analysis of the field observations in Sec. 3 shows a strong correlation between melt pond reflectance and color with under-pond SIT. Accordingly, we can develop an empirical under-pond SIT retrieval based on these observations and YIQ color space results. However, we exclude the Quadrature component Q as the analysis shows that it does not contain complementary

https://doi.org/10.5194/egusphere-2026-7079
Preprint. Discussion started: 24 November 2026
© Author(s) 2026. CC BY 4.0 License.

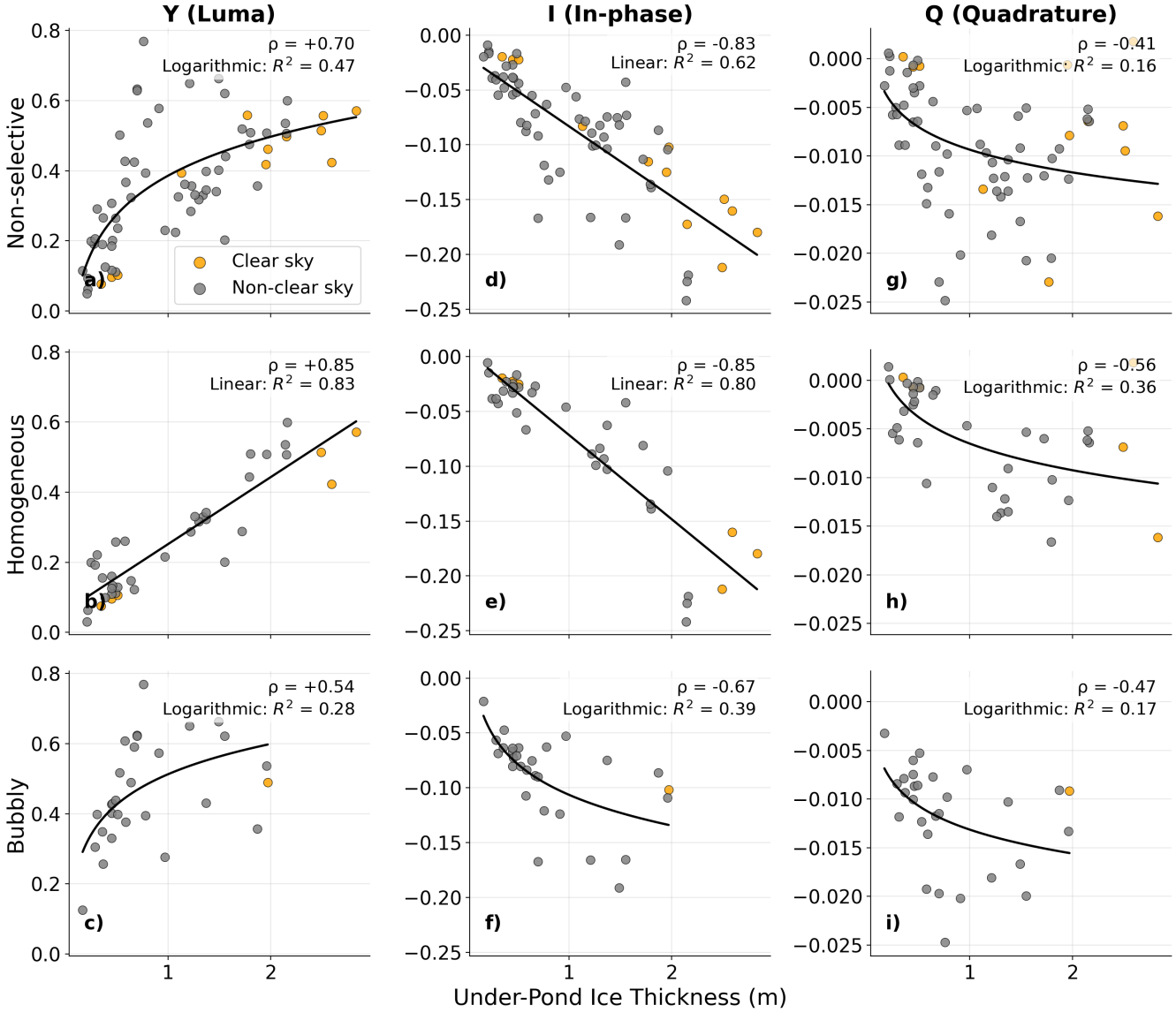

Figure 11. The scatter plots show the YIQ (Luma-In-phase-Quadrature) color space components of all melt pond measurements plotted against the co-located under-pond SIT measurements. The black lines show the one dimensional least squares fits. Panels a), d) and g) show the results for the full dataset, panels b), e) and h) for the homogeneous-bottom sub-dataset and c), f) and i) for the bubbly-bottom sub-dataset. The orange colored markers specify the measurements during clear-sky conditions, the grey colored markers specify the measurements during non-clear sky conditions. The corresponding Spearman rank correlation coefficient ρ, indicating the correlation of the individual color space parameter with under-pond sea ice thickness, is shown in the upper right of each subplot. The R^2 value refers to the least squares fit and indicates how much of the variation within the data is explained by it.

https://doi.org/10.5194/egusphere-2026-7079
Preprint. Discussion started: 24 November 2026
© Author(s) 2026. CC BY 4.0 License.

information and has significantly weaker correlations with under-pond SIT (H_i). Therefore, we use a two-dimensional (2D) bivariate linear regression fit (we later also use the term model) based on the Luma Y and In-Phase I component for the retrieval in the general form: $H_i = aY + bI + c$. Note that all previous figures within this study display the reflectance R or color parameter Y, I or Q as a function of under-pond SIT: $R = f(H_i)$; $Y, I, Q = f(H_i)$. However, in order to derive fits for an under-pond SIT retrieval we have to use the inverse relation meaning the x- and y-axis of the previous figures are switched to get the following relation where Y and I are used as proxies for under-pond SIT: $H_i = f(Y, I)$. Instead of using only one universal fit we use individual fits for each melt pond bottom type dataset to explore the potential of a retrieval which can distinguish between those bottom types. As the bubbly-bottom and non-selective-dataset measurements show a logarithmic increase for Y (Fig. 11) with increasing under-pond SIT - meaning an exponential increase in the inverse relationship - Y is replaced by $\exp(Y)$ as the first predictor for these two datasets: $H_i = a \cdot \exp(Y) + bI + c$. This substitution increases the predictive skill of the 2D fits significantly (not shown). The resulting individual 2D linear regression fits for all three melt pond bottom types are:

$$\text{Non-selective:} \quad H_i = -0.60 \cdot \exp(Y) - 11.97\, I + 0.91, \tag{3}$$

$$\text{Homogeneous:} \quad H_i = 2.83\, Y - 3.93\, I + 0.02, \tag{4}$$

$$\text{Bubbly:} \quad H_i = -0.63 \cdot \exp(Y) - 10.06\, I + 0.92. \tag{5}$$

All three individual models are evaluated in Fig. 12 by applying each to all measurements. Accordingly, this represents an in-sample validation and not a validation against measurements independent from the training data. The purpose here is to verify how well the models describe their training data. The deviations from the 1:1 line directly indicate the internal retrieval uncertainty based on the selected fits. The coefficient of determination (R^2), root mean square error (RMSE) and mean absolute error (MAE) are shown in the lower right corner of each subplot. Apart from the last two error metrics, R^2 is a key measure to quantify retrieval performance, as it represents the fraction of variance in the measured under-pond SIT explained by the model prediction. In the lower row of the figure the relative errors of all models averaged for 0.5 m bins are displayed.

Of all three models the homogeneous-bottom model (Eq. 4) achieves the highest retrieval skill, with an R^2 of 0.85, RMSE of 0.30 m, and MAE of 0.21 m (Fig. 12b). The bubbly-bottom model (Eq. 5, Fig. 12c) only achieves relatively low retrieval skill with $R^2 = 0.31$ (RMSE = 0.42 m, MAE = 0.31 m). The non-selective-dataset model (Eq. 3, Fig. 12a) achieves intermediate performance with $R^2 = 0.64$ (RMSE = 0.42 m, MAE = 0.34 m) which is slightly lower than the one reported by Lu et al. (2018) ($R^2 = 0.67$) but higher than the R^2 of Malinka et al. (2018) ($R^2 = 0.56$), both of which did not differentiate between pond bottom types. Comparing the MAE and RMSE of our models, which range from 0.21–0.34 m and 0.30–0.42 m, respectively, with the uncertainty range of ±0.1–0.7 m reported for common Arctic SIT retrievals (Sect. 1) suggests that our model errors are of a comparable magnitude to retrieval uncertainties. However, note that our performance metrics reflect in-sample fit, whereas those reported in other studies are partly based on validation against independent measurements.

https://doi.org/10.5194/egusphere-2026-7079
Preprint. Discussion started: 24 November 2026
© Author(s) 2026. CC BY 4.0 License.

All three models show a tendency to overestimate thin under-pond SIT below 1 m and to underestimate thicker under-pond SIT above (Fig. 12 d-f). The models have the highest mean relative errors (MRE) for under-pond SIT below 0.5 m with values reaching up to +75 %. This is expected as we do not have a minimum SIT defined. Therefore, the MRE goes to infinity when the under-pond SIT approaches zero. However, the MAE is below 0.25 m for all three models below 1 m under-pond SIT. While the bubbly-bottom model underestimates under-pond SIT above 1 m by up to -45 % (Fig. 12f) the homogeneous-bottom (Fig. 12e) as well as the non-selective model (Fig. 12d) only show up to -30 % underestimation. The MAE of both, the non-selective model (Fig. 12d) and the bubbly-bottom model (Fig. 12f) reach values of up to 0.8 m while the MAE of the homogeneous-bottom model stays below 0.65 m (Fig. 12e). However, the range of observed under-pond SIT for bubbly-bottom cases is confined to below 2 m only allowing for a limited comparison with the other two models.

The models are further evaluated using leave-one-pond-out cross-validation. All sampling positions and repeated visits from one physical pond are withheld together. The models are refitted using the remaining ponds and used to predict thickness for the omitted pond. The non-selective model (12 ponds) achieves a held-out RMSE of 0.5 m and $R^2 = 0.5$. The homogeneous model (11 ponds) achieves an RMSE of 0.36 m and $R^2 = 0.78$. The homogeneous model retains most of its performance. The non-selective model shows a moderate decline. The bubbly model (7 ponds) shows a substantial decrease in performance with a held-out RMSE of 1.07 m and $R^2 = -3.36$. Accordingly, the results of this cross-validation indicate poorer predictive performance and limited transferability for bubbly pond bottoms. However, mind that with 7 ponds also less data is available for the fit for the bubbly model compared to the other two (11 & 12 ponds). The non-selective and homogeneous models show relatively stable predictions and more reliable transfer across ponds.

In general these results confirm that the presented color-based SIT retrieval approach is competitive with previous model- and observation-based retrievals while operating only on YI measurements. Our results further show that, for spatially sufficiently resolved hyperspectral observations, retrieval skill can be substantially improved by classifying the pond bottom type prior to applying the corresponding type-specific model — a refinement not employed in previous studies. The spectral slope method described in Sect. 3.1.2 can be used for such a pre-retrieval bottom classification.

Several limitations of this retrieval approach should be acknowledged. Retrieval performance may be affected by in-camera processing of the input images. Processed images, such as JPEGs, should be encoded in the *AdobeRGB* color space and linearized to ensure consistency with the training data used here (Sect. 2.3).
The retrieval relationships were derived from nadir observations of melt ponds and have not been evaluated for oblique viewing geometries. Furthermore, all melt pond measurements analyzed here represent surfaces with 100% melt pond coverage. Retrieval performance decreases substantially when the input measurements contain a mixture of pond, ice, and ocean surfaces (not shown).
This limitation means that applying the presented retrievals to imagery with coarser spatial resolution requires a melt pond fraction (MPF) retrieval to identify pixels with an MPF close to 100%. Combined with an MPF retrieval, the under-pond SIT

https://doi.org/10.5194/egusphere-2026-7079
Preprint. Discussion started: 24 November 2026
© Author(s) 2026. CC BY 4.0 License.

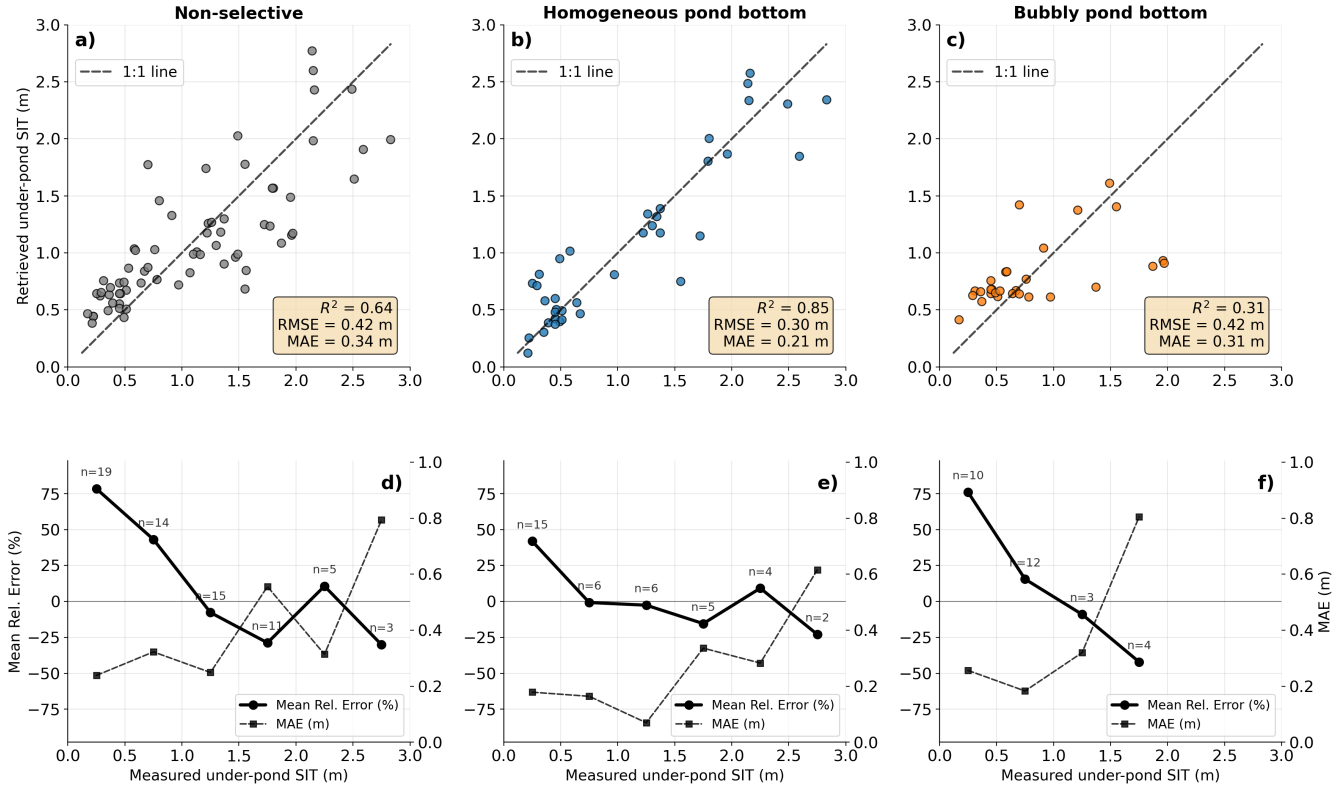

Figure 12. (a)-(c): Scatter plots of model-retrieved vs. measured under-pond SIT for the three YI regression models. (Eqs. 3–5). The dashed line represents the 1:1 relationship. (d)-(f): Mean relative and mean absolute errors of the three models averaged for 0.5 m bins of under-pond SIT. n indicates the number of measurements within each bin.

retrieval can be applied to airborne RGB imagery acquired by drones and aircraft. Application to satellite imagery is theoretically possible but additionally requires cloud masking and atmospheric correction and is therefore beyond the scope of the present approach.

5 Conclusions

Within this study we present a new extensive dataset of 67 hyperspectral melt pond images co-located with under-pond SIT and melt pond depth measurements. The measurements cover a variety of different melt ponds on first-year and multiyear ice as well as the full range of typical Arctic summer SIT (0–3 m). The subsequent analysis of this dataset not only proofs that it offers promising possibilities to study melt pond reflectance and albedo with regard to under-pond SIT and melt pond depth. It also demonstrates the value of the dataset for validating existing and future melt pond reflectance models.

https://doi.org/10.5194/egusphere-2026-7079
Preprint. Discussion started: 24 November 2026
© Author(s) 2026. CC BY 4.0 License.

Our measurements confirm previous model studies that under-pond SIT is the dominating factor influencing melt pond reflectance. It further underlines the importance of melt pond bottom structure in controlling the shape of the reflectance - under-pond SIT relationship. Especially, the observed near-linear relationship of homogeneous melt pond bottom ice thickness and reflectance has not been reported in previous literature.

Regarding the non-selective (i.e. mixed) pond bottoms our measurements are in good agreement with the simulated melt pond reflectance of the Malinka et al. (2018) model. But the model cannot reproduce the linear relationship of the homogeneous pond bottoms as it is assuming a saturating hyperbolic function for melt pond reflectance. Therefore, we suggest to evaluate if and how other melt pond reflectance models, such as the ones from Lu et al. (2016) and Zhang et al. (2021), are able to reproduce the different reflectance - under-pond SIT relationships for different melt pond bottom types. Despite the good agreement between model and observations for the non-selective pond bottoms it might be of value to incorporate the linear reflectance relationship for homogeneous pond bottoms in melt pond reflectance models. This could be of benefit for local sea ice transmissivity and ecosystem studies using such melt pond reflectance models.

We further demonstrated that melt pond bottoms with enclosed air bubbles have a more negative mean spectral reflectance slope within the range of 690–730 nm than homogeneous bottoms. A spectral slope threshold of -0.002 nm^{-1} can be used to automatically detect bubbly melt pond bottoms and improve the accuracy of retrieving under-pond SIT.

Finally, we showed that the YIQ color space offers promising potential for under-pond SIT retrieval. As it separates luminance from chrominance it is a better predictor for under-pond SIT than the RGB color space. From our measurements, converted to the YIQ color space, we derived two dimensional bivariate linear regression fits in dependence of Y and I for each of the three analyzed melt pond bottom categories. All models show RMSE and MAE values of less than 0.42 m and 0.34 m, respectively, making them competitive to other Arctic SIT retrievals. The homogeneous model showed particularly promising results, with an R^2 value of 0.85. Leave-one-pond-out cross-validation indicated promising stability for the homogeneous and non-selective models. The bubbly model, based on only seven ponds, showed poor transferability. A broader calibration dataset and further independent validation are therefore needed before applying this specific pond-bottom model to other datasets. In general, these results underline the promising capability of adding crucial summer SIT estimates by retrieving the ice thickness below melt ponds.

Future work will be focused on validating this retrieval approach by other independent melt pond observations and to develop an under-pond SIT retrieval for air- and space-borne platforms.

https://doi.org/10.5194/egusphere-2026-7079
Preprint. Discussion started: 24 November 2026
© Author(s) 2026. CC BY 4.0 License.



Data availability. The hyperspectral images are available from PANGAEA (Ringel et al., 2026). The accompanying *CSV* file lists the image IDs used in the analysis and the areas selected for spectral averaging. The co-located measurements of under-pond sea ice thickness and melt pond depth will be archived on PANGAEA by Clemens-Sewall et al. (2026, in prep.).

Appendix A: Appendix A

Table A1. Comparison of drilled and GEM-derived under-pond sea ice thickness (SIT) at five waypoints along the GEM transect across *R1_droneTwoPond*. Δ = GEM estimate − measured. All values in m.

	Waypoint					Statistics	
	2 m	7 m	15 m	28 m	33 m	Mean	Std
Under-pond SIT, drilled [m]	1.070	0.220	0.230	0.210	0.700	0.486	0.387
Under-pond SIT, GEM [m]	0.716	0.389	0.116	0.308	0.698	0.445	0.259

	2 m	7 m	15 m	28 m	33 m	Bias	MAE	RMSE
Δ under-pond SIT [m]	−0.354	0.169	−0.114	0.098	−0.002	−0.041	0.147	0.188

Table A2. Least-squares fits of reflectance R versus under-pond sea ice thickness H_i (m) at 400, 600 and 800 nm for the three pond bottom types shown in Fig. 6 and introduced in Sec.1 & 3.1.1. n is the number of spectra. For homogeneous pond bottoms, both a linear and a logarithmic fit are given for comparison.

Pond bottom	n	H_i range (m)	λ (nm)	Fit	Equation	R^2
Mixed	67	0.17–2.83	400	log	$R = 0.476 + 0.213 \ln(H_i)$	0.54
			600	log	$R = 0.304 + 0.113 \ln(H_i)$	0.38
			800	log	$R = 0.075 + 0.025 \ln(H_i)$	0.19
Homogeneous	38	0.21–2.83	400	linear	$R = 0.062 + 0.260\, H_i$	0.85
			400	log	$R = 0.393 + 0.242 \ln(H_i)$	0.76
			600	linear	$R = 0.063 + 0.131\, H_i$	0.79
			600	log	$R = 0.230 + 0.125 \ln(H_i)$	0.74
			800	linear	$R = 0.025 + 0.018\, H_i$	0.33
			800	log	$R = 0.048 + 0.017 \ln(H_i)$	0.29
Bubbly	29	0.17–1.97	400	log	$R = 0.608 + 0.159 \ln(H_i)$	0.33
			600	log	$R = 0.423 + 0.092 \ln(H_i)$	0.23
			800	log	$R = 0.092 + 0.016 \ln(H_i)$	0.12

https://doi.org/10.5194/egusphere-2026-7079
Preprint. Discussion started: 24 November 2026
© Author(s) 2026. CC BY 4.0 License.

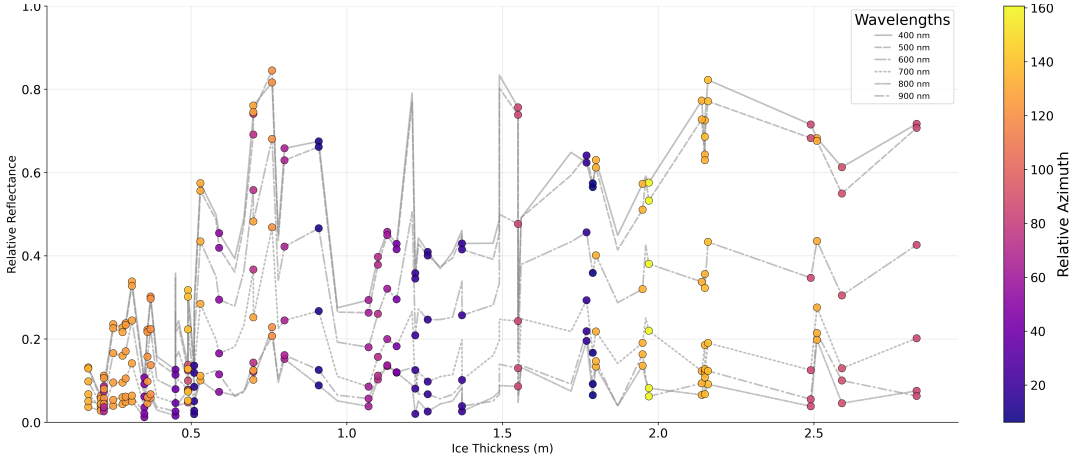

Figure B1. Same plot as shown by Fig. 6 for the non-selective dataset but markers are color-coded by the relative azimuth angle (°) between the camera and the sun during the measurement.

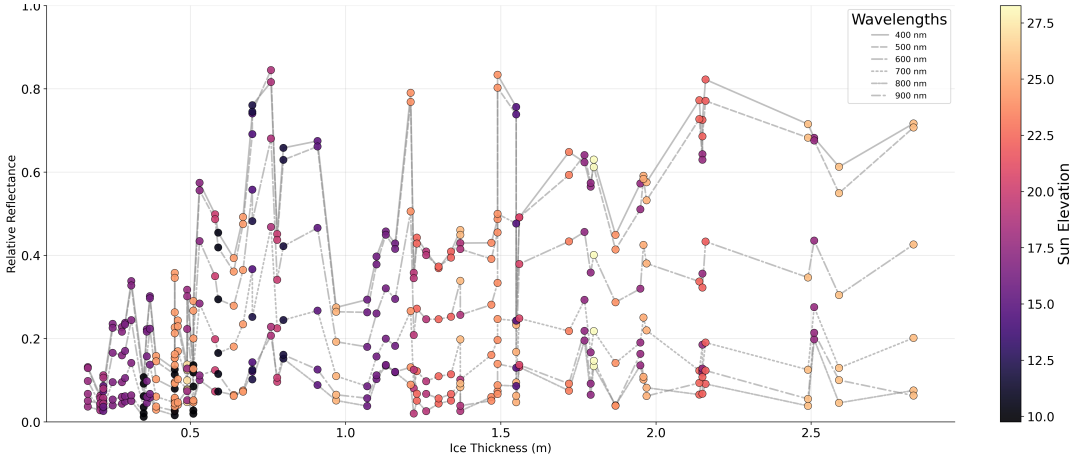

Figure B2. Same plot as shown by Fig. 6 for the non-selective dataset but markers are color-coded by the sun elevation angle (°) during the measurement.

Appendix B: Appendix B

https://doi.org/10.5194/egusphere-2026-7079
Preprint. Discussion started: 24 November 2026
© Author(s) 2026. CC BY 4.0 License.

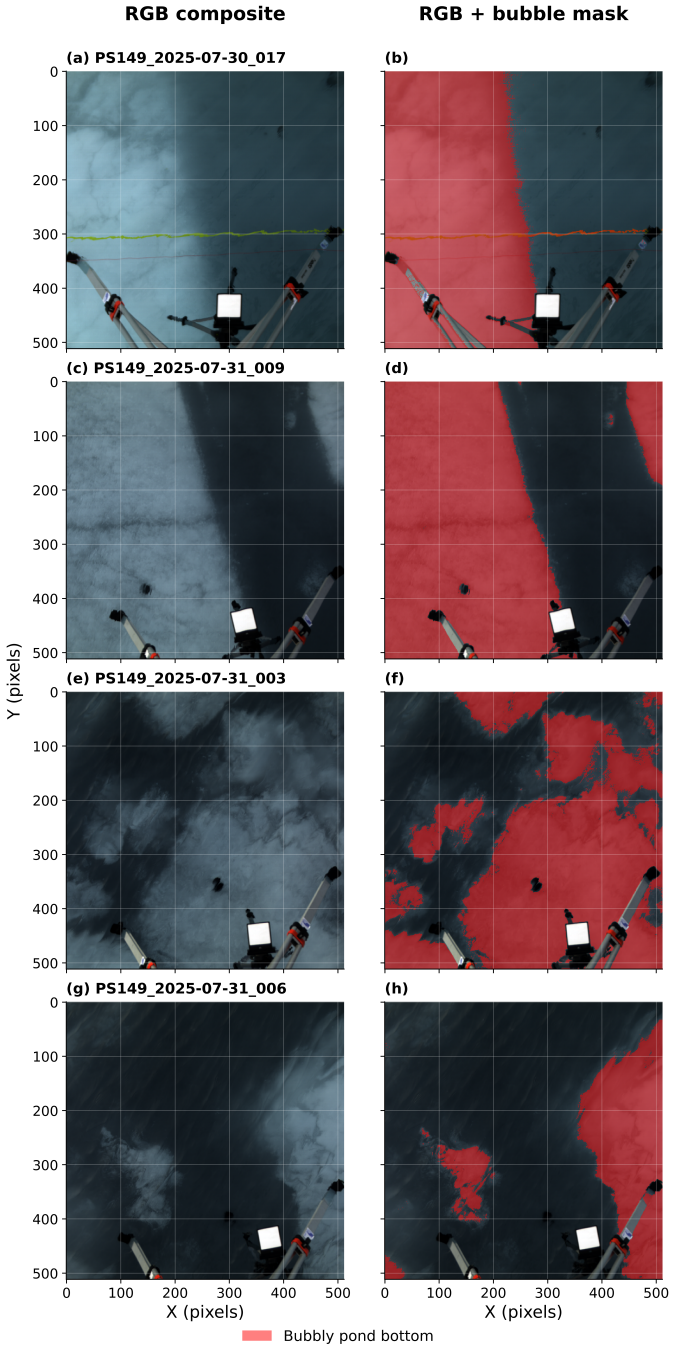

Figure B3. Additional examples of the application of the spectral slope criterion (Sect. 3.1.2, Fig. 9) to a selection of hyperspectral images covering bubbly melt pond bottom.

https://doi.org/10.5194/egusphere-2026-7079
Preprint. Discussion started: 24 November 2026
© Author(s) 2026. CC BY 4.0 License.

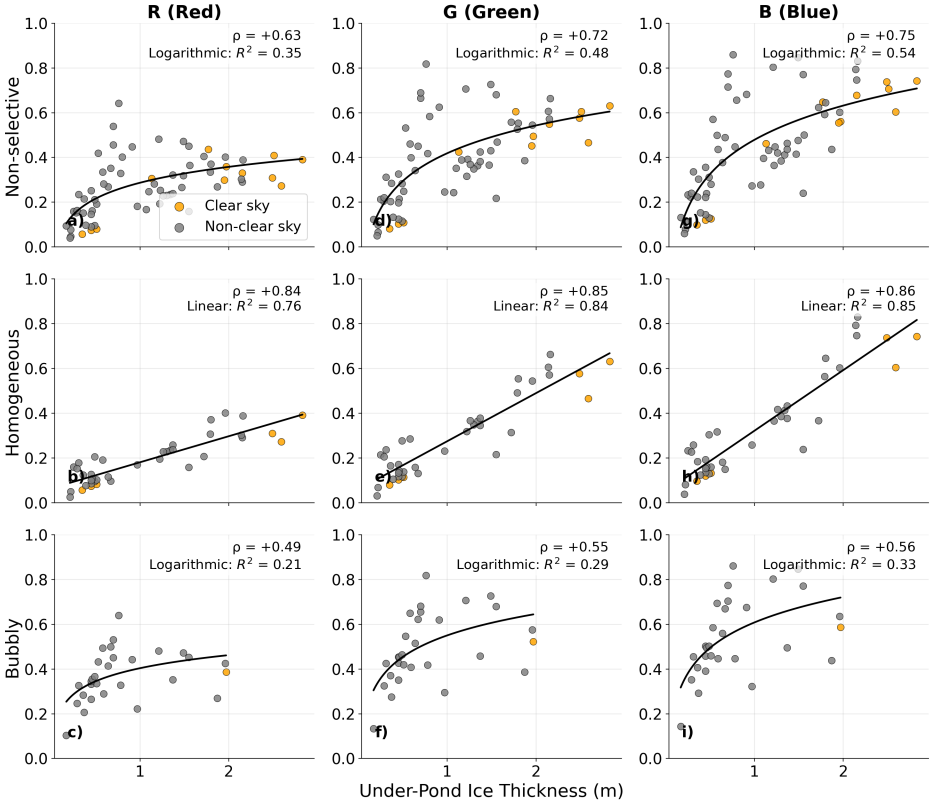

Figure B4. Same figure as Fig. 11 in Sect. 3.2.2 bug for the RGB color space.

B1

Author contributions. Maximilian Harald Ringel (MR), Gunnar Spreen and Janna Rückert developed the study concept. MR analyzed the data, and wrote the initial paper draft. MR and Gunnar Spreen conducted the field measurements with support from Marcel Nicolaus, Melinda A. Webster, David Clemens-Sewall, and Dimitry Divine. All authors participated in discussions, provided critical feedback, and contributed to the manuscript text.

Competing interests. The contact author has declared that none of the authors has any competing interests.

Acknowledgements. We gratefully acknowledge the funding by the Deutsche Forschungsgemeinschaft (DFG, German Research Foundation) - Projektnummer 268020496 - TRR 172, within the Transregional Collaborative Research Center "ArctiC Amplification: Climate Relevant

https://doi.org/10.5194/egusphere-2026-7079
Preprint. Discussion started: 24 November 2026
© Author(s) 2026. CC BY 4.0 License.

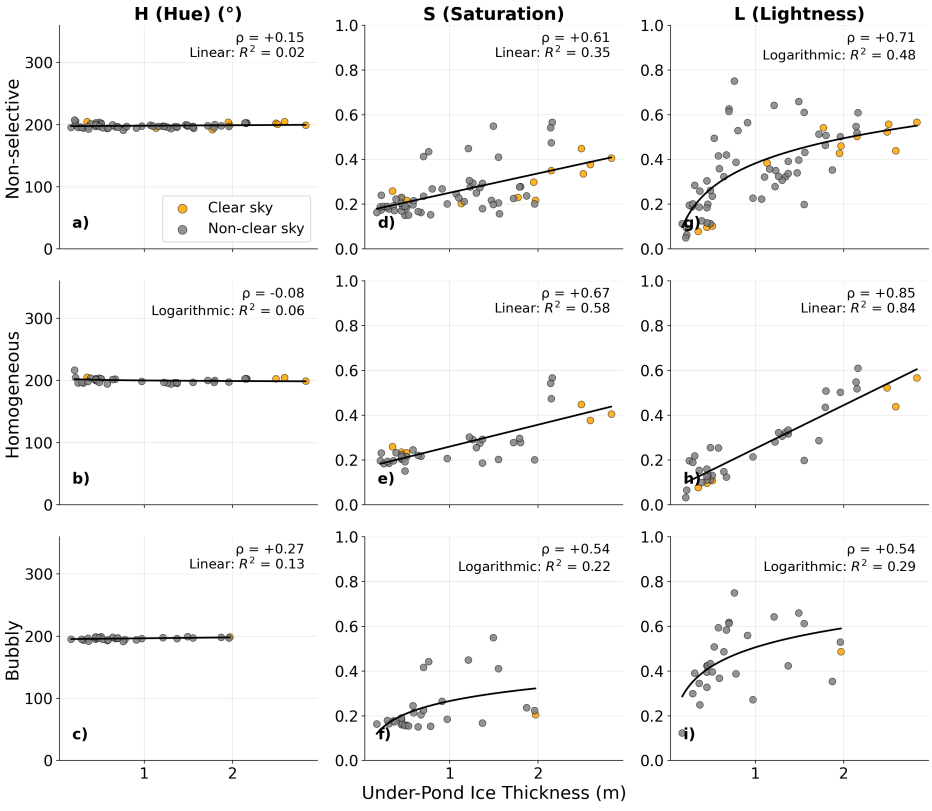

Figure B5. Same figure as Fig. 11 in Sect. 3.2.2 bug for the HSL (Hue, Saturation, Luminance) color space.

Atmospheric and SurfaCe Processes, and Feedback Mechanisms (AC)3".

We thankfully acknowledge the following people for supporting our measurements in the field during the CONTRASTS (PS149) expedition: Linxin Zhang, Linnu Bühler, Phillip Eisenhuth, Stefanie Brechtelsbauer, Nora Greenwood, Savannah Byron, and Johannes Gerstein. We further thank all persons involved in the expedition of the research vessel *Polarstern* during *CONTRASTS* in 2025 (AWI_PS149_00).

We used different AI model versions of *ChatGPT* and *Claude* to improve the clarity and concision of author-written text, reorganize selected paragraphs, and assist with coding. The authors were fully responsible for the scientific analysis, interpretation, and conclusions.

https://doi.org/10.5194/egusphere-2026-7079
Preprint. Discussion started: 24 November 2026
© Author(s) 2026. CC BY 4.0 License.

References

Akino, R., Nomura, D., Webb, A., Li, Y., Dall'osto, M., Schmidt, K., Droste, E. S., Chamberlain, E. J., Kolabutin, N., Shimanchuk, E., Dadic, R., Fong, A. A., Torres-Valdés, S., Hoppe, C. J. M., Whitmore, L., Meyer, H., Nosaka, Y., Inoue, J., Müller, O., and Delille, B.: Melt Pond Nutrient Dynamics and Their Relationship With Melt Pond Bottom Ice in the Central Arctic Ocean, J. Geophys. Res.-Oceans, 130, e2024JC022018, https://doi.org/10.1029/2024jc022018, 2025.

Ardyna, M., Mundy, C. J., Mayot, N., Matthes, L. C., Oziel, L., Horvat, C., Leu, E., Assmy, P., Hill, V., Matrai, P. A., Gale, M., Melnikov, I. A., and Arrigo, K. R.: Under-Ice Phytoplankton Blooms: Shedding Light on the "Invisible" Part of Arctic Primary Production, Front. Mar. Sci., 7, 608032, https://doi.org/10.3389/fmars.2020.608032, 2020a.

Ardyna, M., Mundy, C. J., Mills, M. M., Oziel, L., Grondin, P.-L., Lacour, L., Verin, G., van Dijken, G., Ras, J., Alou-Font, E., Babin, M., Gosselin, M., Tremblay, J.-É., Raimbault, P., Assmy, P., Nicolaus, M., Claustre, H., and Arrigo, K. R.: Environmental drivers of under-ice phytoplankton bloom dynamics in the Arctic Ocean, Elem. Sci. Anth., 8, 30, https://doi.org/10.1525/elementa.430, 2020b.

Arrigo, K. R., Perovich, D. K., Pickart, R. S., Brown, Z. W., van Dijken, G. L., Lowry, K. E., Mills, M. M., Palmer, M. A., Balch, W. M., Bahr, F., Bates, N. R., Benitez-Nelson, C., Bowler, B., Brownlee, E., Ehn, J. K., Frey, K. E., Garley, R., Laney, S. R., Lubelczyk, L., Mathis, J., Matsuoka, A., Mitchell, B. G., Moore, G. W. K., Ortega-Retuerta, E., Pal, S., Polashenski, C. M., Reynolds, R. A., Schieber, B., Sosik, H. M., Stephens, M., and Swift, J. H.: Massive Phytoplankton Blooms Under Arctic Sea Ice, Science, 336, 1408–1408, https://doi.org/10.1126/science.1215065, 2012.

Cao, X., Lu, P., Lei, R., Wang, Q., and Li, Z.: Physical and optical characteristics of sea ice in the Pacific Arctic Sector during the summer of 2018, Acta Oceanol. Sin., 39, 25–37, https://doi.org/10.1007/s13131-020-1645-6, 2020.

Colour Developers: Colour Science for Python, version 0.4.7, PyPI [code], https://pypi.org/project/colour-science/0.4.7/, 2025.

Dawson, G., Landy, J., Tsamados, M., Komarov, A. S., Howell, S., Heorton, H., and Krumpen, T.: A 10-year record of Arctic summer sea ice freeboard from CryoSat-2, Remote Sens. Environ., 268, 112 744, https://doi.org/10.1016/j.rse.2021.112744, 2022.

Grenfell, T. C. and Perovich, D. K.: Spectral albedos of sea ice and incident solar irradiance in the southern Beaufort Sea, J. Geophys. Res.-Oceans, 89, 3573–3580, https://doi.org/10.1029/jc089ic03p03573, 1984.

Grenfell, T. C. and Perovich, D. K.: Incident spectral irradiance in the Arctic Basin during the summer and fall, J. Geophys. Res.-Atmos., 113, D12117, https://doi.org/10.1029/2007jd009418, 2008.

Haas, C. and Jochmann, P.: Continuous EM and ULS thickness profiling in support of ice force measurements, in: Proceedings of the 17th International Conference on Port and Ocean Engineering under Arctic Conditions, pp. 849–856, Trondheim, Norway, https://hdl.handle.net/10013/epic.19621.d001, 2003.

Haas, C., Gerland, S., Eicken, H., and Miller, H.: Comparison of sea-ice thickness measurements under summer and winter conditions in the Arctic using a small electromagnetic induction device, Geophysics, 62, 749–757, https://doi.org/10.1190/1.1444184, 1997.

Haas, C., Lobach, J., Hendricks, S., Rabenstein, L., and Pfaffling, A.: Helicopter-borne measurements of sea ice thickness, using a small and lightweight, digital EM system, J. Appl. Geophys., 67, 234–241, https://doi.org/10.1016/j.jappgeo.2008.05.005, 2009.

Hendricks, S., Itkin, P., Ricker, R., Webster, M., von Albedyll, L., Rohde, J., Raphael, I., Jaggi, M., and Arndt, S.: GEM-2 quicklook total thickness measurements from the 2019-2020 MOSAiC expedition, PANGAEA [data set], https://doi.org/10.1594/PANGAEA.943666, 2022.

Huntemann, M., Heygster, G., Kaleschke, L., Krumpen, T., Mäkynen, M., and Drusch, M.: Empirical sea ice thickness retrieval during the freeze-up period from SMOS high incident angle observations, Cryosphere, 8, 439–451, https://doi.org/10.5194/tc-8-439-2014, 2014.

https://doi.org/10.5194/egusphere-2026-7079
Preprint. Discussion started: 24 November 2026
© Author(s) 2026. CC BY 4.0 License.

Istomina, L., Melsheimer, C., Huntemann, M., Nicolaus, M., and Heygster, G.: Retrieval of sea ice thickness during melt season from in situ, airborne and satellite imagery, in: 2016 IEEE International Geoscience and Remote Sensing Symposium (IGARSS), pp. 7678–7681, IEEE, https://doi.org/10.1109/igarss.2016.7731002, 2016.

Istomina, L., Niehaus, H., and Spreen, G.: Updated Arctic melt pond fraction dataset and trends 2002–2023 using ENVISAT and Sentinel-3 remote sensing data, Cryosphere, 19, 83–105, https://doi.org/10.5194/tc-19-83-2025, 2025.

Itkin, P., Hendricks, S., Webster, M., von Albedyll, L., Arndt, S., Divine, D., Jaggi, M., Oggier, M., Raphael, I., Ricker, R., Rohde, J., Schneebeli, M., and Liston, G. E.: Sea ice and snow characteristics from year-long transects at the MOSAiC Central Observatory, Elem. Sci. Anth., 11, 00048, https://doi.org/10.1525/elementa.2022.00048, 2023.

Kacimi, S. and Kwok, R.: Two Decades of Arctic Sea-Ice Thickness from Satellite Altimeters: Retrieval Approaches and Record of Changes (2003–2023), Remote Sens., 16, 2983, https://doi.org/10.3390/rs16162983, 2024.

Karvonen, J., Cheng, B., Vihma, T., Arkett, M., and Carrieres, T.: A method for sea ice thickness and concentration analysis based on SAR data and a thermodynamic model, Cryosphere, 6, 1507–1526, https://doi.org/10.5194/tc-6-1507-2012, 2012.

Katlein, C., Nicolaus, M., and Petrich, C.: The anisotropic scattering coefficient of sea ice, J. Geophys. Res.-Oceans, 119, 842–855, https://doi.org/10.1002/2013jc009502, 2014.

Kurtz, N. T., Farrell, S. L., Studinger, M., Galin, N., Harbeck, J. P., Lindsay, R., Onana, V. D., Panzer, B., and Sonntag, J. G.: Sea ice thickness, freeboard, and snow depth products from Operation IceBridge airborne data, Cryosphere, 7, 1035–1056, https://doi.org/10.5194/tc-7-1035-2013, 2013.

Landrum, L. L. and Holland, M. M.: Influences of changing sea ice and snow thicknesses on simulated Arctic winter heat fluxes, Cryosphere, 16, 1483–1495, https://doi.org/10.5194/tc-16-1483-2022, 2022.

Landy, J. C., Dawson, G. J., Tsamados, M., Bushuk, M., Stroeve, J. C., Howell, S. E. L., Krumpen, T., Babb, D. G., Komarov, A. S., Heorton, H. D. B. S., Belter, H. J., and Aksenov, Y.: A year-round satellite sea-ice thickness record from CryoSat-2, Nature, 609, 517–522, https://doi.org/10.1038/s41586-022-05058-5, 2022.

Laxon, S. W., Giles, K. A., Ridout, A. L., Wingham, D. J., Willatt, R., Cullen, R., Kwok, R., Schweiger, A., Zhang, J., Haas, C., Hendricks, S., Krishfield, R., Kurtz, N., Farrell, S., and Davidson, M.: CryoSat-2 estimates of Arctic sea ice thickness and volume, Geophys. Res. Lett., 40, 732–737, https://doi.org/10.1002/grl.50193, 2013.

Lee, S., Stroeve, J., Webster, M., Fuchs, N., and Perovich, D. K.: Inter-comparison of melt pond products from optical satellite imagery, Remote Sens. Environ., 301, 113 920, https://doi.org/10.1016/j.rse.2023.113920, 2024.

Light, B., Grenfell, T. C., and Perovich, D. K.: Transmission and absorption of solar radiation by Arctic sea ice during the melt season, J. Geophys. Res.-Oceans, 113, C03023, https://doi.org/10.1029/2006jc003977, 2008.

Light, B., Perovich, D. K., Webster, M. A., Polashenski, C., and Dadic, R.: Optical properties of melting first-year Arctic sea ice, J. Geophys. Res.-Oceans, 120, 7657–7675, https://doi.org/10.1002/2015jc011163, 2015.

Lu, P., Leppäranta, M., Cheng, B., and Li, Z.: Influence of melt-pond depth and ice thickness on Arctic sea-ice albedo and light transmittance, Cold Reg. Sci. Technol., 124, 1–10, https://doi.org/10.1016/j.coldregions.2015.12.010, 2016.

Lu, P., Leppäranta, M., Cheng, B., Li, Z., Istomina, L., and Heygster, G.: The color of melt ponds on Arctic sea ice, Cryosphere, 12, 1331–1345, https://doi.org/10.5194/tc-12-1331-2018, 2018.

Malinka, A., Zege, E., Istomina, L., Heygster, G., Spreen, G., Perovich, D., and Polashenski, C.: Reflective properties of melt ponds on sea ice, Cryosphere, 12, 1921–1937, https://doi.org/10.5194/tc-12-1921-2018, 2018.

https://doi.org/10.5194/egusphere-2026-7079
Preprint. Discussion started: 24 November 2026
© Author(s) 2026. CC BY 4.0 License.

Melling, H. and Riedel, D. A.: The underside topography of sea ice over the continental shelf of the Beaufort Sea in the winter of 1990, J. Geophys. Res.-Oceans, 100, 13 641–13 653, https://doi.org/10.1029/95jc00309, 1995.

Mobley, C., Cota, G., Grenfell, T., Maffione, R., Pegau, W., and Perovich, D.: Modeling light propagation in sea ice, IEEE Trans. Geosci. Remote Sens., 36, 1743–1749, https://doi.org/10.1109/36.718642, 1998.

Morassutti, M. P. and Ledrew, E. F.: Albedo and Depth of Melt Ponds on Sea-Ice, Int. J. Climatol., 16, 817–838, https://doi.org/10.1002/(sici)1097-0088(199607)16:7<817::aid-joc44>3.0.co;2-5, 1996.

Nicolaus, M.: The Expedition PS149 of the Research Vessel POLARSTERN to the Arctic Ocean in 2025, Berichte zur Polar- und Meeresforschung 808, Alfred Wegener Institute, Helmholtz Centre for Polar and Marine Research, https://doi.org/10.57738/BZPM_0808_2026, 2026.

Nicolaus, M., Katlein, C., Maslanik, J., and Hendricks, S.: Changes in Arctic sea ice result in increasing light transmittance and absorption, Geophys. Res. Lett., 39, L24501, https://doi.org/10.1029/2012gl053738, 2012.

Niehaus, H., Istomina, L., Nicolaus, M., Tao, R., Malinka, A., Zege, E., and Spreen, G.: Melt pond fractions on Arctic summer sea ice retrieved from Sentinel-3 satellite data with a constrained physical forward model, Cryosphere, 18, 933–956, https://doi.org/10.5194/tc-18-933-2024, 2024.

Notz, D. and Stroeve, J.: Observed Arctic sea-ice loss directly follows anthropogenic CO_2 emission, Science, 354, 747–750, https://doi.org/10.1126/science.aag2345, 2016.

Oziel, L., Massicotte, P., Randelhoff, A., Ferland, J., Vladoiu, A., Lacour, L., Galindo, V., Lambert-Girard, S., Dumont, D., Cuypers, Y., Bouruet-Aubertot, P., Mundy, C.-J., Ehn, J., Bécu, G., Marec, C., Forget, M.-H., Garcia, N., Coupel, P., Raimbault, P., Houssais, M.-N., and Babin, M.: Environmental factors influencing the seasonal dynamics of spring algal blooms in and beneath sea ice in western Baffin Bay, Elem. Sci. Anth., 7, 34, https://doi.org/10.1525/elementa.372, 2019.

Paţilea, C., Heygster, G., Huntemann, M., and Spreen, G.: Combined SMAP–SMOS thin sea ice thickness retrieval, Cryosphere, 13, 675–691, https://doi.org/10.5194/tc-13-675-2019, 2019.

Perovich, D. K.: Observations of the polarization of light reflected from sea ice, J. Geophys. Res.-Oceans, 103, 5563–5575, https://doi.org/10.1029/97jc01615, 1998.

Perovich, D. K.: Complex yet translucent: the optical properties of sea ice, Physica B, 338, 107–114, https://doi.org/10.1016/s0921-4526(03)00470-8, 2003.

Perovich, D. K. and Polashenski, C.: Albedo evolution of seasonal Arctic sea ice, Geophys. Res. Lett., 39, L08501, https://doi.org/10.1029/2012gl051432, 2012.

Perovich, D. K., Roesler, C. S., and Pegau, W. S.: Variability in Arctic sea ice optical properties, J. Geophys. Res.-Oceans, 103, 1193–1208, https://doi.org/10.1029/97jc01614, 1998.

Perovich, D. K., Grenfell, T. C., Light, B., and Hobbs, P. V.: Seasonal evolution of the albedo of multiyear Arctic sea ice, J. Geophys. Res.-Oceans, 107, SHE 20–1–SHE 20–13, https://doi.org/10.1029/2000jc000438, 2002.

Petty, A., Kurtz, N. T., Kwok, R., Markus, T., and Neumann, T. A.: Winter Arctic Sea Ice Thickness From ICESat-2 Freeboards, J. Geophys. Res.-Oceans, 125, e2019JC015764, https://doi.org/10.1029/2019jc015764, 2020.

Petty, A., Cabaj, A., and Landy, J. C.: Initial assessment of all-season Arctic sea ice thickness from ICESat-2, J. Glaciol., 72, e4, https://doi.org/10.1017/jog.2025.10119, 2026.

Pfaffling, A., Haas, C., and Reid, J. E.: Direct helicopter EM — Sea-ice thickness inversion assessed with synthetic and field data, Geophysics, 72, F127–F137, https://doi.org/10.1190/1.2732551, 2007.

https://doi.org/10.5194/egusphere-2026-7079
Preprint. Discussion started: 24 November 2026
© Author(s) 2026. CC BY 4.0 License.

Python Software Foundation: colorsys module in the Python 3.13.5 standard library, CPython repository [code], https://raw.githubusercontent.com/python/cpython/v3.13.5/Lib/colorsys.py, 2025.

Reid, J. E. and Vrbancich, J.: A comparison of the inductive-limit footprints of airborne electromagnetic configurations, Geophysics, 69, 1229–1239, https://doi.org/10.1190/1.1801939, 2004.

Ringel, M. H., Spreen, G., and Huntemann, M.: Hyperspectral camera raw data (SPECIM IQ 01) of nadir melt pond images taken during the RV Polarstern PS149 CONTRASTS cruise (July-August 2025), PANGAEA [data set], https://doi.org/10.1594/PANGAEA.995758, 2026.

Rothrock, D. A. and Wensnahan, M.: The Accuracy of Sea Ice Drafts Measured from U.S. Navy Submarines, J. Atmos. Ocean. Tech., 24, 1936–1949, https://doi.org/10.1175/jtech2097.1, 2007.

Smith, R. C. and Baker, K. S.: Optical properties of the clearest natural waters (200–800 nm), Appl. Opt., 20, 177–184, https://doi.org/10.1364/ao.20.000177, 1981.

Spreen, G., de Steur, L., Divine, D., Gerland, S., Hansen, E., and Kwok, R.: Arctic Sea Ice Volume Export Through Fram Strait From 1992 to 2014, J. Geophys. Res.-Oceans, 125, e2019JC016039, https://doi.org/10.1029/2019jc016039, 2020.

Stroeve, J. and Notz, D.: Changing state of Arctic sea ice across all seasons, Environ. Res. Lett., 13, 103 001, https://doi.org/10.1088/1748-9326/aade56, 2018.

Sumata, H., de Steur, L., Divine, D. V., Granskog, M. A., and Gerland, S.: Regime shift in Arctic Ocean sea ice thickness, Nature, 615, 443–449, https://doi.org/10.1038/s41586-022-05686-x, 2023.

Thomas, D. N., ed.: Sea Ice: Its Physics, Chemistry, Biology, Geology and Societal Importance, Wiley, Hoboken, NJ, 4th edn., ISBN 9781394213757, https://doi.org/10.1002/9781394213764, 2025.

Tian-Kunze, X., Kaleschke, L., Maaß, N., Mäkynen, M., Serra, N., Drusch, M., and Krumpen, T.: SMOS-derived thin sea ice thickness: algorithm baseline, product specifications and initial verification, Cryosphere, 8, 997–1018, https://doi.org/10.5194/tc-8-997-2014, 2014.

Webster, M. A., Arndt, S., Bliss, A., Kacimi, S., Maksym, T., Massonnet, F., Riihelä, A., and Toyota, T.: Changes in Arctic and Antarctic sea-ice properties and processes, Nat. Rev. Earth Environ., 7, 688–707, https://doi.org/10.1038/s43017-026-00816-9, 2026.

Welch, H. E.: A Year on the Ice: The SHEBA/JOIS Project, ARCTIC, 51, 293–300, https://doi.org/10.14430/arctic1071, 1998.

Xiong, C. and Ren, Y.: Arctic sea ice melt pond fraction in 2000–2021 derived by dynamic pixel spectral unmixing of MODIS images, ISPRS J. Photogramm. Remote Sens., 197, 181–198, https://doi.org/10.1016/j.isprsjprs.2023.01.023, 2023.

Youden, W. J.: Index for rating diagnostic tests, Cancer, 3, 32–35, https://doi.org/10.1002/1097-0142(1950)3:1<32::AID-CNCR2820030106>3.0.CO;2-3, 1950.

Yu, Y. and Rothrock, D. A.: Thin ice thickness from satellite thermal imagery, J. Geophys. Res.-Oceans, 101, 25 753–25 766, https://doi.org/10.1029/96jc02242, 1996.

Zege, E., Malinka, A., Katsev, I., Prikhach, A., Heygster, G., Istomina, L., Birnbaum, G., and Schwarz, P.: Algorithm to retrieve the melt pond fraction and the spectral albedo of Arctic summer ice from satellite optical data, Remote Sens. Environ., 163, 153–164, https://doi.org/10.1016/j.rse.2015.03.012, 2015.

Zhang, H., Yu, M., Lu, P., Zhou, J., and Li, Z.: Retrievals of Arctic sea ice melt pond depth and underlying ice thickness using optical data, Adv. Polar Sci., 32, 105–117, https://doi.org/10.13679/j.advps.2021.0021, 2021.

Zhang, H., Lu, P., Yu, M., Zhou, J., Wang, Q., Li, Z., and Zhang, L.: Comparison of Pond Depth and Ice Thickness Retrieval Algorithms for Summer Arctic Sea Ice, Remote Sens., 14, 2831, https://doi.org/10.3390/rs14122831, 2022.